

# Optical Engineering

OpticalEngineering.SPIEDigitalLibrary.org

## **Review of high fidelity imaging spectrometer design for remote sensing**

Pantazis Mouroulis  
Robert O. Green

# Review of high fidelity imaging spectrometer design for remote sensing

Pantazis Mouroulis\* and Robert O. Green

Jet Propulsion Laboratory, California Institute of Technology, Pasadena, California, United States

**Abstract.** We review the design and assessment techniques that underlie a number of successfully deployed space and airborne imaging spectrometers that have been demonstrated to achieve demanding specifications in terms of throughput and response uniformity. The principles are illustrated with telescope designs as well as spectrometer examples from the Offner and Dyson families. We also show how the design space can be extended with the use of freeform surfaces and provide additional design examples with grating as well as prism dispersive elements. © 2018 Society of Photo-Optical Instrumentation Engineers (SPIE) [DOI: [10.1117/1.OE.57.4.040901](https://doi.org/10.1117/1.OE.57.4.040901)]

Keywords: imaging spectroscopy; spectrometer; optical design; space instrumentation; remote sensing; freeform design.

Paper 180023V received Jan. 4, 2018; accepted for publication Apr. 2, 2018; published online Apr. 26, 2018.

## 1 Introduction

Spectroscopy is a key analytical method used to investigate material composition and related processes through study of the interaction of light with matter. Isaac Newton described the spectral nature of light. Joseph von Fraunhofer invented the spectroscope in 1814 and used it to characterize the optical properties of glass for the development of more powerful telescopes. He also identified the dark lines in the solar spectrum. Kirchhoff and Bunsen used spectroscopy to investigate the composition of the solar atmosphere by establishing the connection between the solar Fraunhofer lines and the spectroscopic signatures of elements observed in the laboratory. Determining composition remotely, without physical contact, is one of the most valuable capabilities of spectroscopy. From this beginning, spectroscopy has evolved and been used to enable a broad range of scientific discoveries by Edwin Hubble to deduce the expanding nature of the universe.

In the late 1970s detector, optical and computer technology advanced sufficiently to enable a class of instrumentation that could measure a spectrum for every point in an image. Development of the Airborne Imaging Spectrometer (AIS) began in 1979 at the NASA Jet Propulsion Laboratory. It was enabled by a newly available  $32 \times 32$  element HgCdTe area detector array from Rockwell Scientific, Inc. (now Teledyne Imaging Sensors Inc.). AIS first flew in 1982 and immediately demonstrated the capability of imaging spectroscopy to measure materials remotely.<sup>1,2</sup> Based on the success of AIS, a more capable instrument, the Airborne Visible-Infrared Imaging Spectrometer (AVIRIS)<sup>3-5</sup> was developed for NASA Earth science. AVIRIS measures the visible to short wavelength infrared (VSWIR), spectral range from 380 to 2510 nm, and first flew in 1986. Figure 1 depicts the imaging spectrometer measurement approach applied at Cuprite, Nevada,<sup>6</sup> for investigation of surface geologic properties via mineral spectral signature.<sup>7</sup> On Earth, AVIRIS and other subsequent imaging spectrometers have been used to pursue a wide range of scientific investigations including

ecosystem canopy chemistry, composition, and function; surface geologic and soil composition; coastal ocean and inland waters properties and benthic composition including corals; snow and ice albedo, grain size, impurities, and melting; fire fuel, combustion, severity, and recovery; atmospheric water vapor, carbon dioxide, methane, cloud phase, and aerosols; anthropogenic infrastructure properties; etc. Examples of many of these research enabling capabilities from imaging spectrometer measurements are given in Ref. 8.

At the same time, as early airborne imaging spectrometers were being developed and tested, NASA and other space agencies realized the value of this type of instrumentation to unambiguously detect, measure, and map molecules/compounds, and investigate processes remotely for science missions throughout the solar system. The near-infrared mapping spectrometer<sup>9</sup> was developed for the Galileo mission to Jupiter and launched in 1989. The visual and infrared mapping spectrometer<sup>10,11</sup> was developed for the Cassini mission to Saturn and launched in 1997. The Hyperion imaging spectrometer<sup>12</sup> was launched as a technology demonstration in 2000 on the Earth Observing 1 mission. ESA launched the compact high resolution imaging spectrometer<sup>13,14</sup> demonstration imaging spectrometer to Earth orbit in 2001, the Observatoire pour la Minéralogie, l'Eau, les Glaces et l'Activité (OMEGA) imaging spectrometer on Mars Express in 2002<sup>15,16</sup> and the MEdium Resolution Imaging Spectrometer (MERIS)<sup>17</sup> on EnviSat also in 2002. The Visible Infra Red Thermal Imaging Spectrometer (VIRTIS) was launched in 2004 on the Rosetta mission to comet 67P/Churyumov-Gerasimenko. In 2005, the Compact Reconnaissance Imaging Spectrometer for Mars (CRISM)<sup>18</sup> was launched on board the Mars Reconnaissance Orbiter (MRO) mission. The NASA Moon Mineral Mapper (M3)<sup>19,20</sup> and the Hyper Spectral Imager (HySI)<sup>21</sup> of the Indian Space Research Organization were launched in 2008 on Chandrayaan-1, India's first mission to the Moon. Nonspace agency imaging spectrometers have also been developed, including the Advanced Responsive Tactically-Effective Military Imaging Spectrometer (ARTEMIS),<sup>22</sup> launched in 2009. Additional imaging spectrometers have been developed

\*Address all correspondence to: Pantazis Mouroulis, E-mail: [pantazis.mouroulis@caltech.edu](mailto:pantazis.mouroulis@caltech.edu)

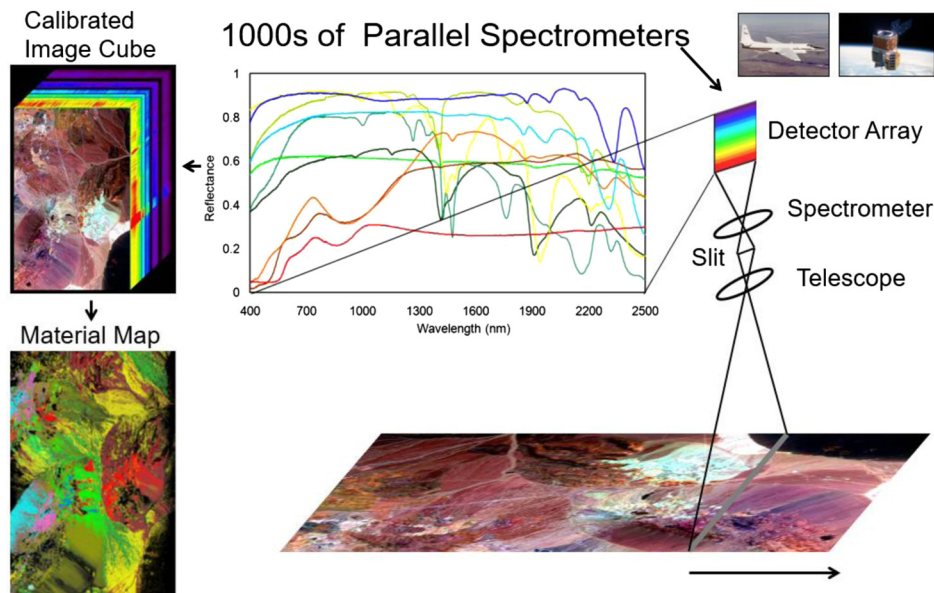


**Fig. 1** Depiction of the imaging spectroscopy measurement approach at the geologically diverse test site at Cuprite, Nevada. A spectrum is acquired for each point in the image. The measured spectra are analyzed for diagnostic mineral absorption features to produce a detailed map of surface mineralogical composition.

and launched for a range of objectives in this timeframe and subsequently. Each of these instruments has a record of key discoveries at their intended destinations. Imaging spectrometers are now routinely included as foundational science instruments for space agency missions throughout the solar system including the Mapping Imaging Spectrometer for Europa (MISE) that is part of NASA's mission to Europa. In addition, configurations are being developed and tested for inclusion on rovers and landers for close proximity investigations as well as *in-situ* surface analysis at the microscopic scale.<sup>23–25</sup> The technology focus for current and future imaging spectrometers is reduced size, mass, and power while delivering improved performance, in terms of spectral, radiometric, spatial, and uniformity characteristics, to be discussed below. Four key elements for successful imaging spectrometer development are (1) design optimization, (2) component fabrication, (3) alignment and calibration, and (4) stability in the operational environment. Specific areas of focus for improved performance in the future are signal-to-noise ratio, calibration, and uniformity. In this paper, the emphasis is on instruments used for remote measurement science through the solar system as well as applications research on Earth. We also limit the review to design forms traditionally known as whiskbroom and pushbroom, where the instantaneous field is either a point or a line, respectively, and henceforth designated as raster-scanning or slit-scanning (where the latter can apply to slit spectrometers regardless of the scan direction). These designs are found in the above-mentioned missions and have also demonstrated high spectroscopic data fidelity.

## 2 Fundamental Design Considerations

The core function of an imaging spectrometer is the identification of materials or ground features through their spectral signature. The imaging aspect is best thought of as a map showing the spatial location of the spectra. By contrast, imaging instruments place the emphasis on spatial content,

which entails the identification of features through their spatial signature (e.g., the shape of a car or building). It is the extraction of accurate spectroscopic information rather than the identification of spatial features that the design of an imaging spectrometer must primarily serve. This has an immediate consequence regarding spatial sampling and resolution, where it is no longer required to sample the optical point spread function (PSF) with more than one detector pixel, as would be the case for a typical imaging system. The features seen by an imaging spectrometer may not be resolved spatially, but the existence of a given material inside a pixel footprint is made evident by the effect of the material on the recovered spectrum.<sup>26,27</sup> Thus, the spatial PSF of an imaging spectrometer is mostly contained inside the detector pixel, and the appearance of the image produced will be pixel-limited in the spatial domain.

Along the spectral direction, the detector pixel size may be a fraction of the slit width if Nyquist or higher sampling is required. However, it has been demonstrated that the higher throughput of critical sampling (pixel width equals slit width) is preferred for the measurement of a wide range of materials.<sup>28</sup> Therefore, a typical imaging spectrometer will provide critical sampling in both the spatial and spectral direction.

Accurate spectroscopic measurement requires high SNR, high calibration accuracy, and high response uniformity. For a given detector and electronic noise level, high SNR is obtained by maximizing the system throughput. This implies an optically fast system with high transmittance. In general, then, a design should seek to minimize the number of optical surfaces as well as provide as low  $F$ -number as possible. Calibration accuracy depends largely on procedures outside the scope of this paper; however, at the design stage, it is important to ensure that accurate calibration is enabled and facilitated by the instrument characteristics. The third requirement, response uniformity, is essentially a restatement

of the following self-evident requirements: that the spectrum of a point on the ground should be independent of where it falls within the field-of-view (FoV) of the spectrometer and that all wavelengths in a spectrum should arise from the same area on the ground. As obvious as these requirements may appear, they have far-reaching consequences for the design of imaging spectrometers, to be explored in detail in the following sections.

Perfect response uniformity is impossible to ensure but the condition can be approximated to a satisfactory level with appropriate care. To understand this, consider first an ideal raster-scanning spectrometer comprising telescope and spectrometer modules connected via an optical fiber. Any point on the ground would have its spectrum measured by the spectrometer, which, in order to avoid time lag, must record the entire spectrum within a single integration time. This can be readily achieved by a linear photodiode array in conjunction with dispersive optics that will spread the spectrum over the array. Sequential wavelength readout from a wavelength-scanning instrument is reserved for essentially stationary applications. Consider next the image of the fiber on the photodiode array. A fraction of the light from the fiber may miss the detector, depending on the fiber core size, photodetector size, spectrometer magnification, and image quality. Evidently, it pays to use a large photodetector array so as to maximize the captured light (although noise/dark current considerations must also be taken into account). For any given pixel size, it is still possible that some light will spill out of the pixel, and for a broadband system covering more than an octave in spectral bandwidth, there will be a significant variation in the diffraction spread between the short and the long wavelengths. It is then possible that more light is lost at the long wavelengths compared to the short wavelengths, which, at an absolute level, produces a spectral error. However, the effect can be accounted for through calibration with a known spectral target so that an accurate spectrum can be recovered for any situation.

In the spatial domain, the fiber core is imaged on the ground by the telescope and determines the sampling distance. Even in the absence of aberrations, the image of the fiber is affected by different diffraction spread between wavelengths. This would violate the uniformity requirement that all wavelengths arise from a fixed area on the ground, unless the diffraction spread can be made small relative to the sample size, leading to an optically fast system. Thus, we see that perfect uniformity can be approximated by a well calibrated raster-scanning instrument in which diffraction (or other chromatic variation) is small relative to the pixel size. The more complicated problem of ensuring uniformity in a slit-scan system is discussed in more detail in the following sections.

### 3 AVIRIS Raster-Scan Design

It is appropriate to start a review of imaging spectrometer design by considering what may be the most successful imaging spectrometer, certainly in terms of utility to the community and in terms of the number of publications and citations it has supported. AVIRIS has been in almost continuous operation since 1987, and, due to a stream of upgrades (documented in the AVIRIS Workshop Proceedings), has retained competitive signal-to-noise ratio (SNR) performance even as alternative technologies were introduced over

the following decades. AVIRIS covers the spectral range from 380 to 2500 nm with spectral sampling of 10 nm, spatial sampling of 1 mrad, and a swath of 34 deg. The key features of the AVIRIS design<sup>29</sup> are: (1) raster-scan architecture, (2) four separate spectrometers, each covering a portion of the entire spectral range, (3) very fast ( $F/1$ ) optics, and (4) large detector pixels (200  $\mu\text{m}$ ), which translates into equally large (200- $\mu\text{m}$  core diameter) fibers placed at the focal plane of the telescope to feed the four spectrometers. The last three features are aimed at maximizing the signal by providing maximum optical throughput and transmittance (grating efficiency). They also make any diffraction spread negligible relative to the detector or fiber size. Maximizing throughput is necessary in order to counteract the limited integration time afforded by the raster-scanning architecture. However, the advantage of this architecture is the corresponding use of linear (as opposed to area) detector arrays, which permits easier and more accurate calibration while minimizing the number of artifacts that plague area array detectors. The use of four separate fibers increases throughput and hence SNR, although it carries the potential of introducing spatial nonuniformity if the four fiber images are not coincident on the ground within a small fraction of a sample.

Little would need to change in the basic AVIRIS architecture if a raster-scan system were to be designed from scratch even today. Different or more compact optics may be possible but that does not alter the fundamental system parameters. In addition, there is a limit to how compact the optics can be since the point-scan design necessitates a large aperture, which in the case of AVIRIS is 200 mm in diameter.

### 4 Slit-Scan Spectrometer Design Fundamentals

The slit-scan sensor images an entire line of ground typically (but not necessarily) in the cross-track direction while the platform provides the forward (along-track) scan. The image of the line, formed on the spectrometer slit, is then dispersed onto a two-dimensional array, which provides spectral information along one axis and spatial along the other. This architecture effectively integrates as many spectrometers as there are cross-track pixels into a single instrument. It therefore permits substantial mass and volume savings, an often definitive advantage especially in resource-constrained space missions. Other potentially significant advantages are the increase in integration time and hence SNR, lack of moving parts, and perhaps reduced polarization sensitivity. In addition, the large increase in integration time permits the use of smaller pixels and optical speeds slower than the extremely demanding  $F/1$  of AVIRIS. A potential disadvantage is the requirement for a wide-field telescope; however, designs exist that provide a wide linear field with excellent correction. A greater concern is the use of an area array detector, which brings problems of uniformity, calibration, readout artifacts, and striping. In this review, we concentrate on the optical aspects of the design process as those are at least amenable to a systematic approach for reducing or removing artifacts before they occur. By contrast, detector and calibration artifacts are typically handled with data postprocessing.

#### 4.1 Characterization

Optical instruments can be characterized by their impulse response or by their frequency response. We have found the impulse response description to be advantageous as it can apply in both the spectral and spatial domain and be readily measurable. The impulse response is also the preferred description used by algorithms that extract information from the raw data. We therefore characterize an imaging spectrometer through its spectral response function (SRF) and its along-track and cross-track spatial response functions (ARF and CRF, respectively). These functions represent the response of the system to either a spectral delta function (SRF) or a spatial point stimulus (ARF and CRF). There is, however, a difference with the proper impulse response: in the spatial domain, the stimulus is not an infinitesimally small point, but rather is presumed to be wide enough to fill the slit or pixel completely. This is a more useful definition for typical extended remote sensing targets though not for stars or similar point targets. Resolution and uniformity are then expressed through these response functions. As is common, we express resolution as a function of the width of the response function, typically the full-width at half-maximum (FWHM).<sup>30</sup>

The presence of the slit complicates the computation of the response functions, since the slit acts as an intermediate diffractive aperture, the effects of which are typically ignored by ray-tracing software. For an accurate computation, one must account for the effects of the slit. If the design satisfies the constraint that the Airy disk diameter for the longest wavelength be smaller than the pixel and slit width, the incoherent approximation can be considered adequate, with the more detailed calculation producing corrections of  $\sim 10\%$ , which are easily consumed within various experimental uncertainties.<sup>31–33</sup>

We consider that the slit length is along the  $x$ -axis, which means that the spectral direction is the  $y$ , as is also the direction of motion. In the incoherent approximation, the SRF depends only on the spectrometer and can be computed starting at the slit, as the convolution of slit (a rect function of width  $y_0$ ),  $y$ -line spread function [ $\text{LSF}_S(y)$ ], and the detector pixel response [Eq. (1)], where the subscript  $S$  stands for spectrometer only, that is, as computed by a raytrace starting at the slit (a grating resolution term shown in previous publications is absorbed in the LSF term). Thus, this is equivalent to flood-illuminating the slit without a telescope. The absence of a real telescope aperture stop and presumed mirror oversizing help approximate that condition closer:

$$\text{SRF} = \text{rect}(y_0) \otimes \text{LSF}_S(y) \otimes \text{DET}(y). \quad (1)$$

The ARF is a function of the telescope only and can be computed as the convolution of the telescope  $y$ -line spread function with the slit width, and an additional rect function (often of the same width) representing the effect of motion blur or integration time [Eq. (2), where subscript  $T$  stands for telescope only, that is, computed at the slit, and subscript  $t$  stands for time]:

$$\text{ARF} = \text{rect}(y_0) \otimes \text{LSF}_T(y) \otimes \text{rect}(y_t). \quad (2)$$

Thus, this is equivalent to receiving the signal on a photo-detector placed immediately behind the slit while neglecting

the spectrometer. However, we approximate the real situation better by analyzing the telescope performance only at the  $F$ -number that is accepted by the spectrometer and neglecting the telescope aperture oversize (telescope aperture size has an effect on radiometry that is accounted separately). Finally, the CRF is computed as the convolution of the combined telescope and spectrometer system ( $x$ -) line spread function with the detector pixel response. This ignores any wavefront clipping at the slit, which, however, is typically a small effect:

$$\text{CRF} = \text{LSF}_{\text{sys}}(x) \otimes \text{DET}(x). \quad (3)$$

It can be seen then that this method of assessment, in addition to being relevant to the data reduction algorithms, also provides a complete assessment of the telescope, the spectrometer, and their combination in a physically meaningful way. The modification of these calculations for a fiber-coupled system should be evident, with both the ARF and CRF being determined by the telescope only, and the partial coherence slit effects not playing a role.

#### 4.2 Uniformity

In a slit-scan sensor, uniformity is a measure of the invariance of the response functions, specifically, invariance of the SRF through field and invariance of the ARF and CRF through wavelength.<sup>30,34</sup> Notice that the variation of the SRF with wavelength or of the CRF/ARF with field is not a uniformity concern as it does not affect the quality of the spectra. A raster-scan sensor in which the spectrum is received on a linear array has inherently perfect spectral uniformity since the spectra for any field location are recorded by the same spectrometer. In a slit-scan sensor, spectral uniformity must be assured by appropriate design and implementation.

Spatial uniformity is not inherently perfect even in a raster-scan sensor as has already been explained. However, the spatial uniformity problem is still generally much easier to handle in a raster-scan sensor, because the slit-scan sensor has to contend with two dimensions that have different characteristics. Specifically, in the CRF direction, the spectrometer module can introduce artifacts, whereas in the raster-scan case, it does not. The CRF can be decoupled from the telescope if a line of fibers is used to connect it to the spectrometer. This solution is not usually preferred as it introduces an additional difficult element to fabricate and can lead to substantial light loss due to less than ideal fiber packing fraction. It may, however, be useful in extreme wide field applications, where it may be difficult to produce a well-behaved line image in any other way.

Uniformity assessment is broken down into geometric and nongeometric aspects, although this is only a convenience that applies to well-designed and implemented instruments with well-behaved single-peaked and reasonably symmetric response functions. The geometric aspects are simple to state. Spectral uniformity demands that the monochromatic image of the slit at any wavelength be straight and aligned with the detector array. Deviation from this condition is often referred to as smile or frown, but it should be clear that the detector alignment, which is not an optical characteristic, must also enter in the final system assessment. Spatial uniformity demands that the spectrometer magnification be

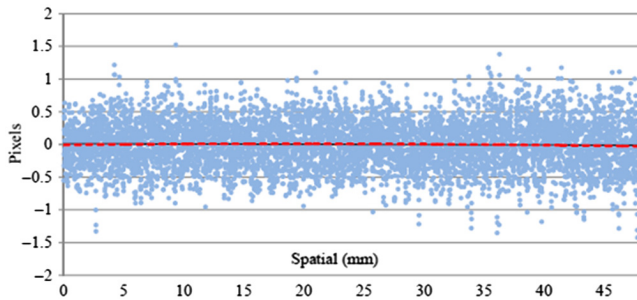


**Fig. 2** Demonstration of very low smile ( $\sim 300$  nm) over a slit length of 48 mm. The points represent centroids of the slit image distribution in the vertical direction. The data were taken with a linear array camera having a pixel size of  $9 \mu\text{m}$ , acting as a line scanner. The design pixel size is  $30 \mu\text{m}$ . The smile assessment can be made confidently to such a low level despite the evident noise, as explained in Ref. 36.

independent of wavelength, so that the slit image is of the same length independent of wavelength; a more complete way to state this is that the polychromatic image of any field point should form a line that is straight and aligned with the detector array. Deviation from this condition is often referred to as keystone, although the trapezoidal shape implied by the term typically fails to describe the actual situation sufficiently.

Deviations from perfect geometric uniformity are measured as a percentage of pixel size across the entire field or wavelength band, respectively. We may speak of a system as 95% uniform or as having a 5% uniformity error. For a short description, instruments are assessed by the worst-case field or wavelength, where nonuniformity occurs, although a more lenient method of assessment would account for the detector area over which the uniformity is achieved in the form of a uniformity map across the entire field and spectrum.

In accordance with tight calibration requirements,<sup>35</sup> deviations from uniformity must be very small, approximately a few percent of a pixel over a scale of many hundreds or thousands of pixels. With appropriate care in the design and execution of an instrument, these tight specifications can be achieved. Figure 2 shows an example of a spectrometer<sup>36</sup> imaging a 48 mm long slit with  $<1\%$  of a  $30\text{-}\mu\text{m}$  pixel smile ( $\sim 300$  nm), and Fig. 3 shows a spatial uniformity of  $\sim 2\%$  over the entire wavelength band of the instrument, 400 to 2500 nm.<sup>37</sup> Although the slit is typically longer than the spectrum spread, the spatial and spectral aspects of the nonuniformity have proven equally hard to satisfy in practice.

We can summarize the geometric aspects of uniformity as the requirement that the first moment (centroid) of the SRF and the CRF must form a perfectly rectangular grid that is aligned with the detector array. The ARF has no role in this assessment.

The nongeometric aspects of uniformity deal with the invariance of the higher moments of the response functions, which can become complicated if those functions are not closely approximated by a simple mathematical form such as a Gaussian.<sup>30,38</sup> To bypass this difficulty, we may note that what actually matters is the variation of the amount of light that spills into the pixels adjacent to the pixel of peak response. Thus, we may simply integrate the light into adjacent pixels and look for the variation, or equivalently, we may characterize the uniformity through a continuous (rather than sampled) variation of the encircled or ensquared energy. Notice that the net amount of light spilling into adjacent pixels is not a uniformity concern, although it may be a resolution concern; it is the chromatic variation of that amount that becomes a spatial uniformity concern, and its spatial variation that becomes a spectral uniformity concern.

To illustrate the point, consider the measured CRF of Portable Remote Imaging Spectrometer (PRISM), an

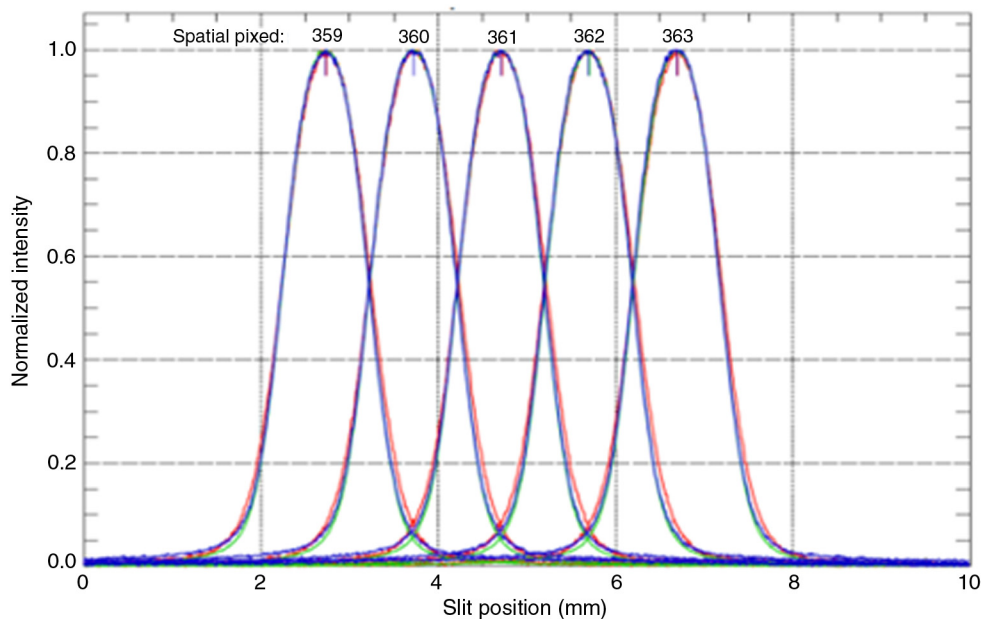


**Fig. 3** Demonstration of high spatial uniformity. The figure shows the CRF of five adjacent pixels over a wavelength range spanning the spectrum of the instrument.<sup>37</sup> Different wavelengths are represented by different colors. Geometric nonuniformity would appear as a displacement of the curves with wavelength.

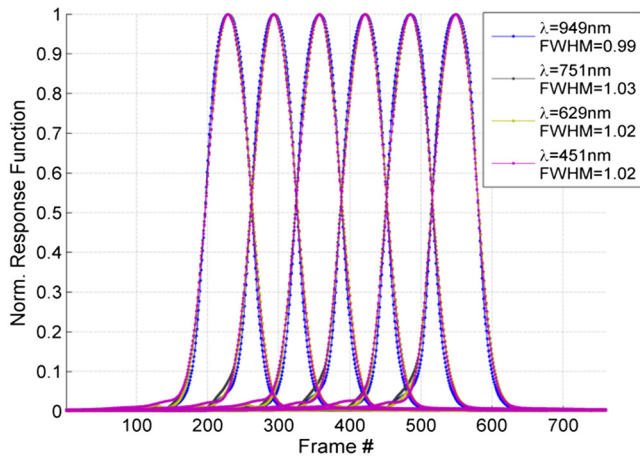


**Fig. 4** Measured CRF of the PRISM demonstrating detector readout artifact (left tail) as a source of asymmetry and thereby deviation from near perfect spatial uniformity.

airborne imaging spectrometer developed for the coastal ocean (Fig. 4).<sup>39</sup> It can be seen that the CRF suffers from asymmetric tails that have a chromatic variation. This is an electronic readout rather than optical artifact, which nevertheless forms part of the total system response and must be accounted for in the uniformity assessment regardless of its source. A more complete and mathematically rigorous form of uniformity assessment has been proposed.<sup>40</sup> The assessment shown here works well enough with well-behaved systems and the response function measurements are relatively straightforward to implement.

## 5 Optical Design Principles

This section deals with the design of the telescope and spectrometer modules separately. This is the way a design normally proceeds. The two separate modules are then added together for the CRF analysis and assessment only. If the aberrations are reasonably corrected in both subsystems, one should expect the CRF to be found adequate.

### 5.1 Telescope Design

There are three fundamental principles or requirements that the telescope design must satisfy: (1) essentially zero transverse chromatic aberration (TCA) or less than a small fraction (such as 1%) of a pixel, (2) minimum (ideally zero) variation of response with wavelength, and (3) maximum transmission. All these requirements must be satisfied for a potentially very wide spectral band, extending over 2.5 octaves or more. In attempting to satisfy these requirements, the designer can make use of the following degrees of freedom (1) that pupil matching between telescope and spectrometer need not be very close provided the telescope aperture is oversized to account for the mismatch, (2) that the telescope need not have a real aperture stop (if not in the thermal infrared range) provided again the mirrors are sufficiently oversized to permit the stop inside the spectrometer to act as the limiting aperture, and (3) that the telescope does not normally need to be diffraction-limited provided the energy is reasonably contained within the pixel—in other words, that maximum spatial resolution is not usually a goal since the spectrometer detects objects through their spectrum rather than their spatial form.

We briefly justify the requirements before considering their implications. Lack of TCA is a geometric uniformity requirement since the aberration produces the same effect as spectrometer keystone. Minimization of the ARF variation with wavelength is also a spatial uniformity requirement of the same type as minimization of the CRF variation for the complete system. Maximum transmission is really a goal that the available photons should not be wasted on their way to the detector, where they would contribute to higher SNR.

The first requirement implies that the telescope will be typically all-reflective so as to have identically zero TCA. Some catadioptric solutions using a refractive field corrector can also be designed with sufficiently small amounts of TCA, although great care needs to be taken in the design. Fully refractive solutions are extremely limited and probably impractical, certainly over a wide spectral band. A few examples have been given in the literature,<sup>41,42</sup> but it can be argued that they fail requirement #3 since the large number of elements reduces transmission due to the difficulty of producing efficient antireflection coatings over a broad band. In any case, it should be clear that one cannot obtain a high-performance imaging spectrometer by attaching a typical camera lens to a spectrometer module.

The second requirement implies that the diffraction spread should be well contained within the pixel or slit width even for the longest wavelength used. This means that the telescope should have a large relative aperture (or low  $F$ -number). For example, a pixel/slit size of  $18\ \mu\text{m}$  at a wavelength of  $2.5\ \mu\text{m}$  implies that the  $F$ -number should be less or considerably less than  $18/(2.44 \times 2.5) = 2.95$ . Again for a broadband system, the diffraction spread is more important than the geometric spot size. To illustrate this, consider two examples, one that has very small spot size and is nearly diffraction-limited even for the short wavelength end and another where there is substantial geometric aberration. Since the telescope is achromatic, the spot size does not change with wavelength but the importance of the geometric aberration does, reducing in significance as the wavelength increases (Fig. 5). The ARF FWHM for the four cases is shown in Table 1.

Evidently, despite the broadening caused by the geometric aberration, the net effect is beneficial in terms of uniformity as the difference in FWHM is considerably smaller in the case of higher aberration (0.6 versus 2.3). However, there is a balancing act to perform since the larger aberration may have an unintended effect on CRF resolution by combining in an unfavorable way with spectrometer aberrations.

### 5.2 Telescope Examples

Several telescope examples exist in the literature that can be used as starting points for the design.<sup>43,44</sup> One of the most common is the three-mirror anastigmat (TMA), of which there are several variations. The two most important variants are a telecentric version with the stop on the secondary and a non-telecentric (or Cook) version, which provides a cold stop location before the image (slit) plane. In practice, the following three designs have been found most useful in satisfying the above requirements over a wide range of applications: the classic TMA, the two-mirror modified Schwarzschild (TMS), and the Cassegrain, typically with a field corrector. Each has a distinct range of applicability. Specifically, the TMS is an unobscured design that can provide the widest

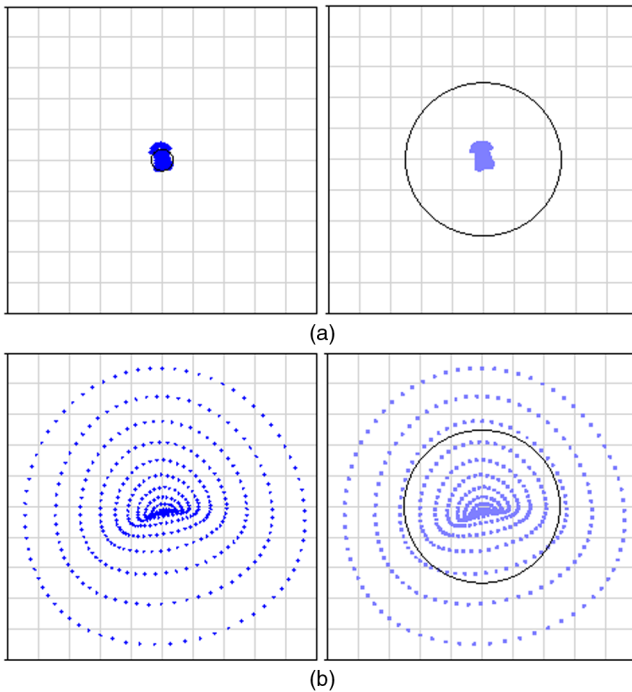


**Fig. 5** Spot diagrams for two achromatic telescopes. The circles show the Airy disk diameters for the shortest and longest wavelength. (a) and (b) Telescope 1 has very low aberration and produces nearly diffraction-limited image even for the short wavelength. (c) and (d) Telescope 2 has higher aberration and more uniform response (Table 1).

**Table 1** ARF FWHM for the PSFs corresponding to Fig. 5.

	Low aberration	Higher aberration
ARF FWHM at 350 nm	30.6	33.0
ARF FWHM at 2500 nm	32.9	33.6

possible field and lowest  $F$ -number, in addition to having the minimum number of mirrors and thus highest transmittance. These are achieved at the expense of a virtual aperture stop and large geometric distortion, which may give pause to a designer but for the fact that these concerns are normally not relevant in imaging spectroscopy. A more significant concern is that the telescope form is essentially an inverted telephoto and therefore large relative to its focal length. For this reason, its application is limited from low to medium resolution and wide field systems.

The TMA can be designed with dimensions roughly equal to its focal length and therefore can be more compact. It can also achieve relatively wide field, though not readily as wide as the TMS. Since focal length and FoV are inversely related (given a fixed detector size and pixel count), this is not so much a disadvantage as a delineation of its range of applicability. However, it cannot normally reach  $F$ -numbers well below 2 because the mirrors are pushed to large off-axis angles to avoid vignetting. For really high resolution (long focal length) applications, the compactness of the Cassegrain design makes it the only choice, however, the basic two-mirror front must be typically followed by either

a refractive or preferably a reflective corrector to widen the field and achieve the final required  $F$ -number. The obscuration and the light loss of this form as well as the larger number of elements are inevitable compromises. A Schmidt corrector plate has also been incorporated,<sup>45</sup> however, its chromatic effect over a broad spectral range would require careful assessment.

To illustrate these points, we show four telescope examples that span a range of applications in terms of FoV,  $F$ -number, and focal length. With the exception of the fourth one, these examples are optimized for a linear field, in which case, no effort is made to correct distortion. This has the result that the image of the slit on the ground is curved; however, this is simply part of the necessary geometric correction that is embedded in the orthorectification model.

The first example (Fig. 6) is a 420 mm  $F/1.8$  TMA with a 16-deg field, designed for an array of  $6400 \times 18 \mu\text{m}$  pixels.<sup>46</sup> This design requires three sixth order aspheres due to the large aperture size. The design is nominally telecentric with the stop at the secondary. Designs with shorter focal length or smaller aperture can readily be scaled down and usually achieve sufficient performance with simpler conic surfaces. This design achieves a average in-pixel ensquared energy of 0.86 and a minimum of 0.83 across the field, or, 92% and 95%, respectively, of the performance of a fully diffraction-limited design. The assessment is made at the longest wavelength, where the ensquared energy is minimum. The corresponding ARF width varies from 1.17 to 1.34, although for any one field point, the variation is smaller, leading to a spatial uniformity of  $\sim 95\%$ .

The second example is a TMS design with a focal length of 24 mm, 50-deg linear FoV at  $F/1.6$ , utilizing one conic (primary mirror) and one fourth order aspheric surface. As there are not enough degrees of freedom in the design, telecentric output can be achieved at the expense of letting the stop location be virtual. This has not been found to be a disadvantage in practical systems as it is generally beneficial to have the telescope aperture be somewhat oversized relative to the spectrometer. The rms spot size achieved varies between 3 and  $6 \mu\text{m}$  across the field (because the pixel size is large for this design, the rms spot size is given instead of ensquared energy). Such performance is hard or impossible to achieve with designs that employ more mirrors,

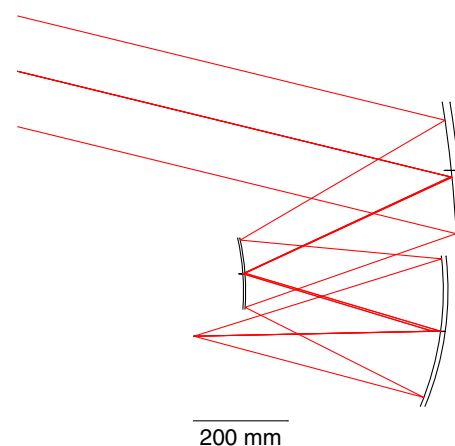


**Fig. 6** A 420-mm  $F/1.8$  TMA with a 16-deg linear FoV (in the plane perpendicular to the page).

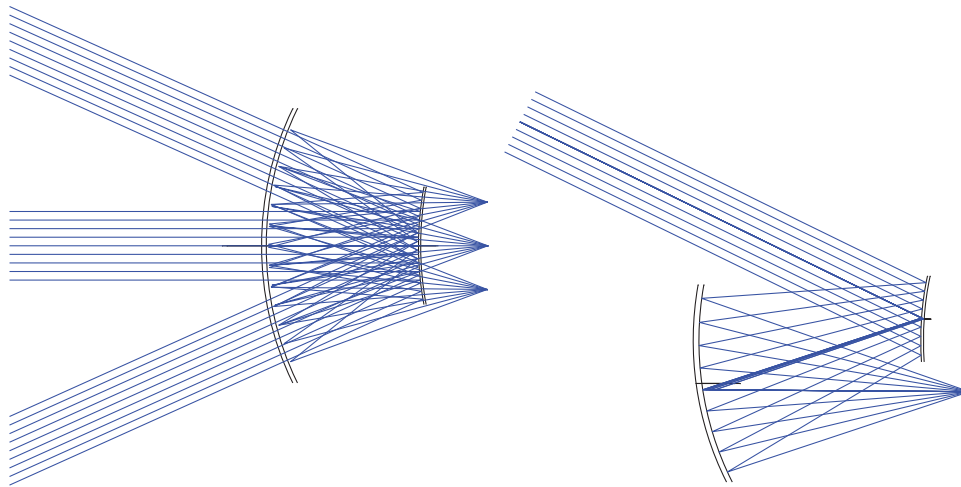


**Fig. 7** Fast two mirror wide-field telescope in two orthogonal views. For telecentric operation, the stop is behind the primary.

so this two-mirror solution represents a unique enabler of otherwise very difficult systems (Fig. 7).

Other designs that have been enabled with this form are a 30 mm  $F/1.4$  with a 33-deg FOV<sup>47</sup> and a 120-mm  $F/1.4$  with a 10-deg FOV. Longer focal length designs are also possible, but they do get large in size as noted.

The third example is a Cassegrain-type design, which becomes necessary for controlling the size when the focal length is very long. In this example, the focal length is 1.75 m and the optical speed is  $F/2.9$  (Fig. 8). The FoV is extended to  $\pm 0.62$  deg, which necessitates a field corrector. This example is included here primarily to demonstrate the required performance of a refractive corrector and by extension any refractive or catadioptric telescope while noting that a reflective corrector is also possible.

The stop is in front of the secondary at the origin of the rays. The field corrector provides also telecentric output. The

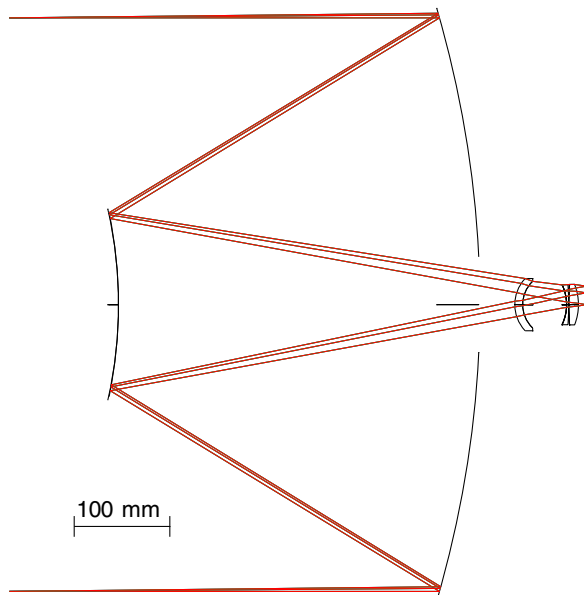


**Fig. 8** A Cassegrain telescope with refractive field corrector.

wavelength range is 380 to 2500 nm. This range limits the available glasses, so the first of the three corrector elements is made of fused silica and the remaining two of  $\text{CaF}_2$ . The FoV corresponds to a slit length of  $1280 \times 30 \mu\text{m}$  (38.4 mm). The corrector takes advantage of the slit field and utilizes an anamorphic (biconic) surface to achieve the required aberration reduction along one direction only. The spot sizes achieved are shown in Fig. 9 and the lateral color in Fig. 10. Maximum lateral color difference is between the two extreme wavelengths and amounts to just under  $1 \mu\text{m}$  at a relative field of  $\sim 0.85$ . This, at 3% of a pixel, is already at the limit of acceptability, thus highlighting the difficulty of obtaining sufficiently achromatized refractive designs for imaging spectroscopy applications.

The fourth example is a 31-mm focal length  $F/1.4$  refractive lens with 37-deg total FoV, operating in the 8 to  $12 \mu\text{m}$  range. The lens is telecentric to match a Dyson type imaging spectrometer, as shown in Sec. 6. Although there is no cold stop, the entire lens can be cooled due to its compact size. Elements have been kept to a minimum thickness to maximize transmittance and reduce mass. The lens and the corresponding spot diagrams are shown in Fig. 11. The total slit length is 20 mm, providing a  $500 (40\times) \mu\text{m}$  pixel swath. In terms of aberrations, the lens is diffraction limited, with the Strehl ratio being 0.93 at the edge of the field and for the shortest wavelength. Distortion in this case does not produce a curved image on the ground, but rather changes the effective instantaneous FoV. It is kept to a maximum of 0.5% across the field. The hardest aberration to control is TCA, which, at just above  $2 \mu\text{m}$ , would be considered very small for any other system except a high-uniformity spectrometer,  $2 \mu\text{m}$  representing 5% of the pixel size. This lens was designed from a catalog of only five, easily available and nonhygroscopic glasses. Expanding the glass catalog would probably result in further reduction of the TCA.

Another way to remove the TCA is shown in Fig. 12, where a TMS wide field front telescope is followed by a 1:1 relay that is exactly symmetric about the stop, and thus immune to TCA. This idea was employed in the HyTES thermal infrared spectrometer design (Sec. 7).

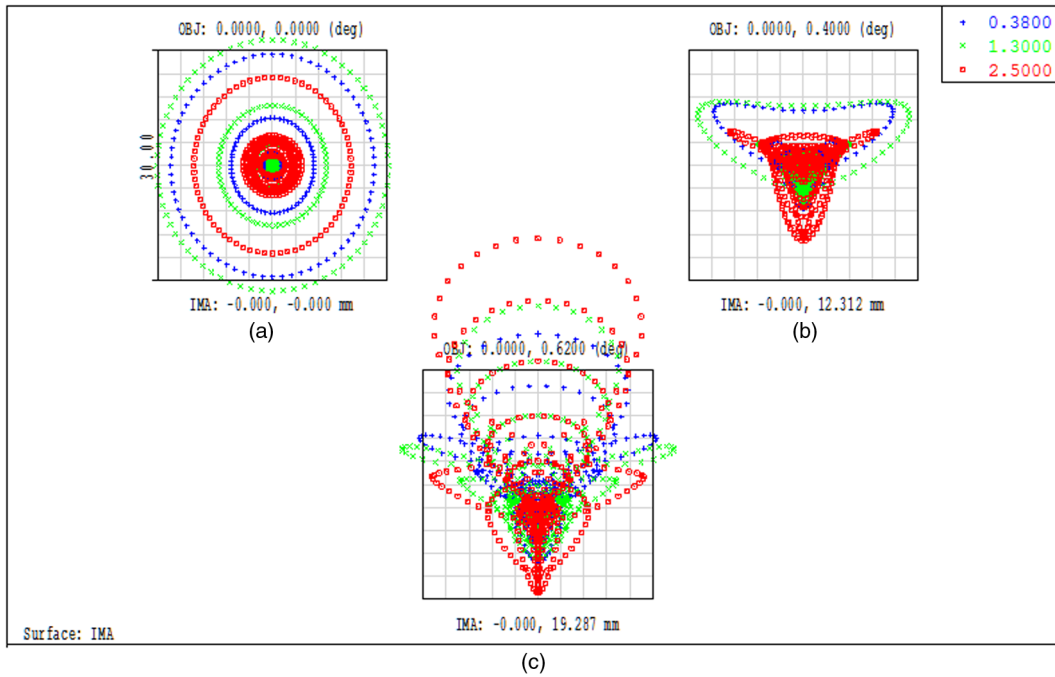


Fig. 9 (a)–(c) Polychromatic (three color) spot diagrams for the telescope of Fig. 8.

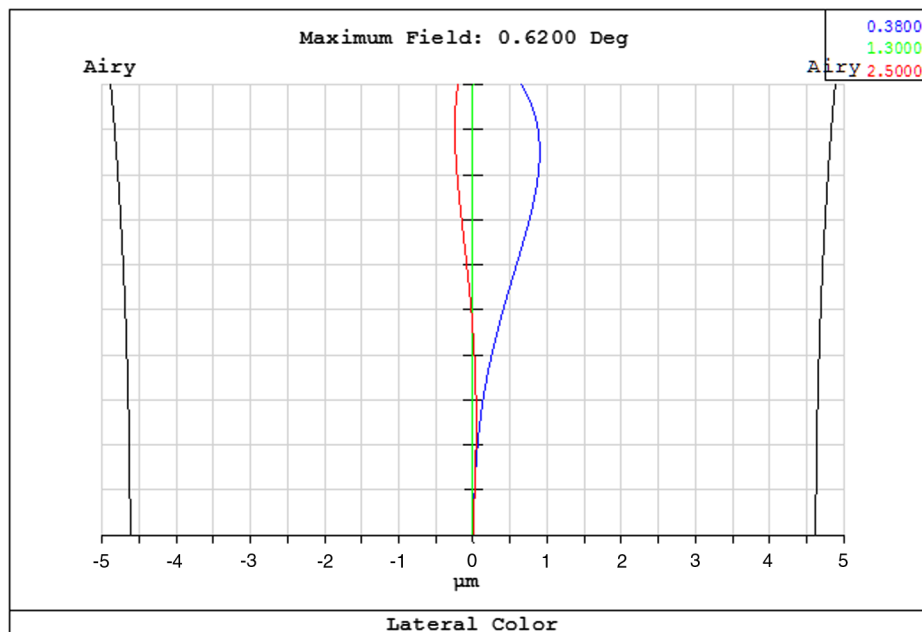
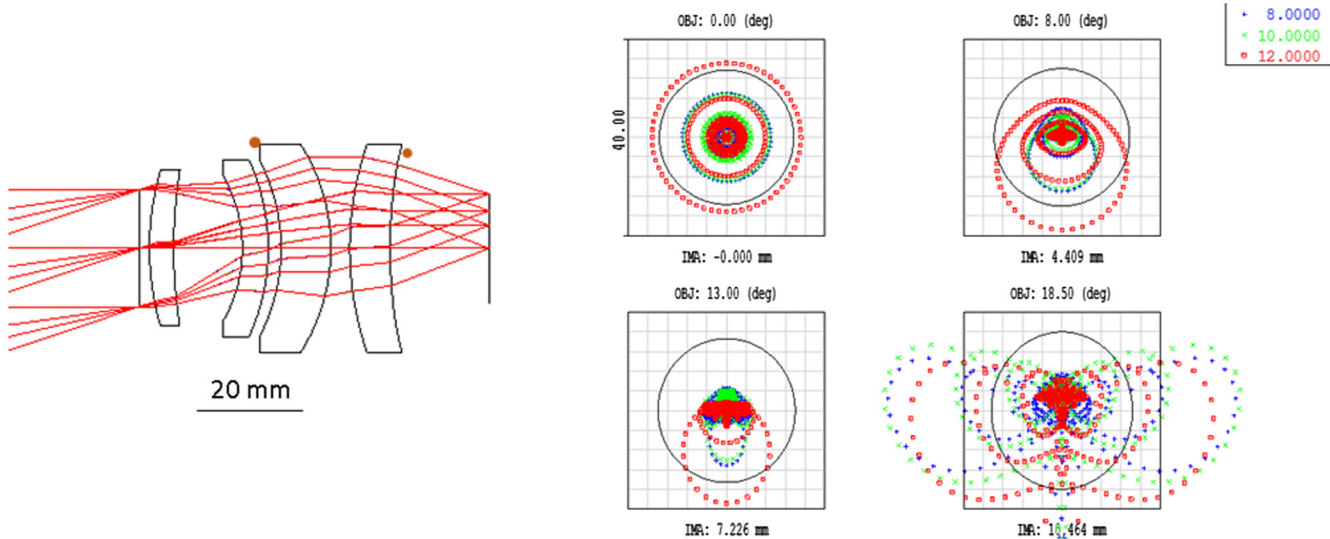


Fig. 10 Lateral color (TCA) as a function of field for the design of Fig. 8. Short and long wavelengths (380 and 2500 nm) are shown relative to the middle (1300 nm). Other wavelengths are in between.

### 5.3 Spectrometer Design

For a successful spectrometer design, it has been found beneficial to adhere to the following principles: (1) geometric distortions should be controlled to  $\sim 1\%$  of a pixel at the design stage (or  $\sim 3\%$  after tolerancing); (2) more than  $\sim 75\%$  of diffraction energy should be contained within the pixel at all wavelengths and fields; (3) degraded spot sizes are acceptable and desirable (subject to rule 2 above) provided they improve uniformity;<sup>48</sup> and (4) the grating or dispersive element is the preferred stop location for

the full system, although if this is not an option, this condition may be violated subject to careful assessment. In addition, two practices that cannot be properly called principles have been found beneficial: (1) integrating the deterministic part of stray light assessment (predictable ghosts and reflections) into the first design pass and (2) assessing uniformity and image quality in terms of CRF, ARF, and SRF, as described previously, while using the more common measures, such as wavefront, spot size, MTF, etc., only as a temporary shortcut if they are much faster to compute, and



**Fig. 11** A  $F/1.4$  diffraction-limited achromatic lens for the thermal infrared range. The aperture stop is at the front. The glasses (from left to right) are GaAs, ZnS, GaAs, and Ge. The two surfaces marked with a dot are conics. The half FoV is 18.5 deg.

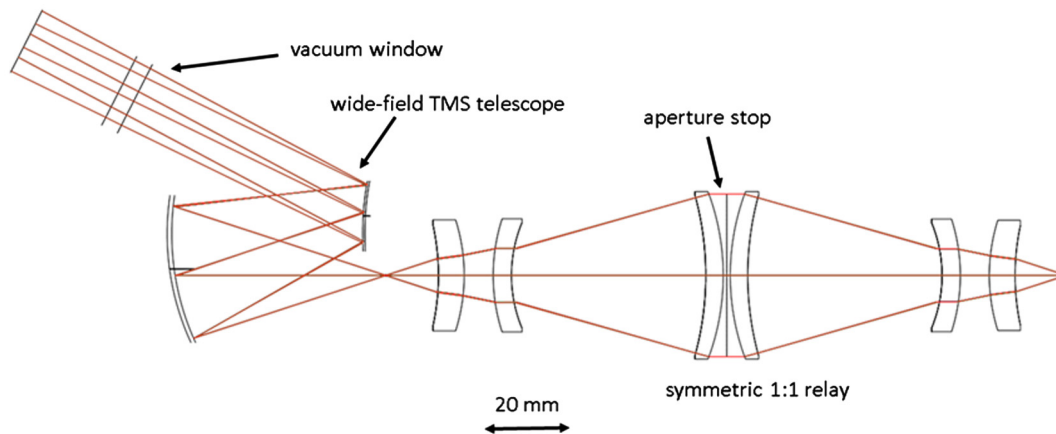


**Fig. 12** A wide-field reflective telescope followed by a refractive 1:1 relay symmetric about the stop has inherently zero TCA. The field of 55 deg is in the plane of the paper. The output is telecentric.

assuming they can be shown to correlate with the response functions.

The implications of these principles are far reaching. Unless the designer incorporates the geometric distortion minimization into the merit function, the tendency of the optical design software will be to correct the point-imaging aberrations often well beyond what is necessary. The inverse of this condition is that a design with well-controlled point-imaging but large geometric nonuniformity may have unacceptable spot sizes once the distortion is corrected. Response uniformity must be enforced at the beginning,<sup>34</sup> and it is for this reason that designs with minimum aberrations but uncontrolled uniformity may not be good starting points for a final uniform design. Such may be the case if one starts from a design form for which the distortion is inherently large and difficult to correct.

#### 5.4 Spectrometer Examples

A major advance in imaging spectrometer design resulted from the Mertz paper<sup>49</sup> showing that concentric relays can

be made into spectrometers by turning the curved mirror at the stop into a grating. The concentric forms have several advantages. They offer a small number of surfaces or optical elements, they are symmetric about the stop, thus offering the potential for minimizing distortion, and can be made to operate at fast optical speeds with good optical correction while also supporting a wide field. In addition, spherical surfaces normally provide sufficient optical correction, with aspheric surfaces required only in extreme cases. The examples shown here are of the concentric type, though it should be clear that deviations from the strict concentric condition are often required.

Consider first a reflective spectrometer of the Offner type<sup>50,51</sup> (Fig. 13). The design has a plane of symmetry along the page. The advantageous orientation of the slit and spectrum relative to this plane depends on which one of the two is longer than the other.<sup>52,53</sup> Typically, the slit is longer, and it is placed perpendicular to the plane of symmetry. The Offner spectrometer is interesting in that it can support any orientation of slit and spectrum by rotating

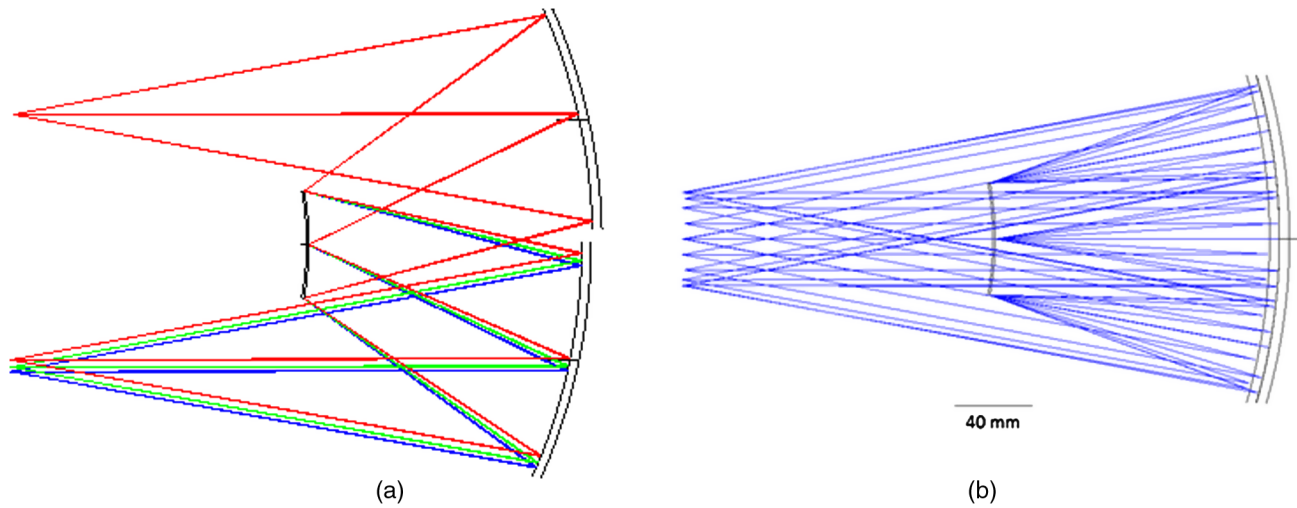


**Fig. 13** A long-slit Offner spectrometer close to the limit of field and aperture size that can be supported with spherical surfaces. (a)  $y-z$  section shows spectrum spread. (b)  $x-z$  section shows slit length.

the grating appropriately. A 45-deg orientation has been studied.<sup>54</sup> The dispersive element need not be a grating. Prism designs have been demonstrated.<sup>55,56</sup> Generally, they cannot approach the level of optical and distortion correction achieved with a grating, but they may be advantageous in cases, where the  $F$ -number is relatively high or the slit not too long.

The Offner spectrometer example of Fig. 13 has the following characteristics: slit length of 48 mm ( $1600 \times 30 \mu\text{m}$  cross-track pixels), optical speed  $F/2.8$ , spectral range 380 to 2500 nm, and spectral sampling of 10 nm/pixel. The design utilizes only spherical surfaces that are test-plated to pre-existing testplates and has a common axis of symmetry for all three surfaces. The longest dimension is 317.4 mm (slit to primary vertex). The grating diameter is 58.2 mm. The design departs from strict concentricity in order to optimize uniformity so that the center of curvature of the third mirror is more than 10 mm away from that of the grating. Also, the grating radius of curvature differs by 3 mm

from the distance between grating vertex and object plane. These seemingly small departures from the ideal Offner relay prescription are critical in producing the desired aberration content for uniformity. The spectrometer has been optimized using the techniques described in Ref. 34. The response uniformity can be appreciated visually using the spot diagrams of Fig. 14. The preferred method of characterization and the spectrometer performance are shown in Table 2, in terms of response function moments and their variation.

In computing the response functions, we assume a Gaussian pixel response function with a FWHM equal to the pixel pitch. This has been found to be a good approximation for some detectors, supported both from direct measurements of the detector MTF and from indirect measurements of the spectrometer system response. Any known or assumed chromatic variation of the FWHM must be folded in here. With the sensors we have used, such variation is typically small.

Much smaller Offner spectrometer examples can be found in the literature, where inevitably the size reduction is

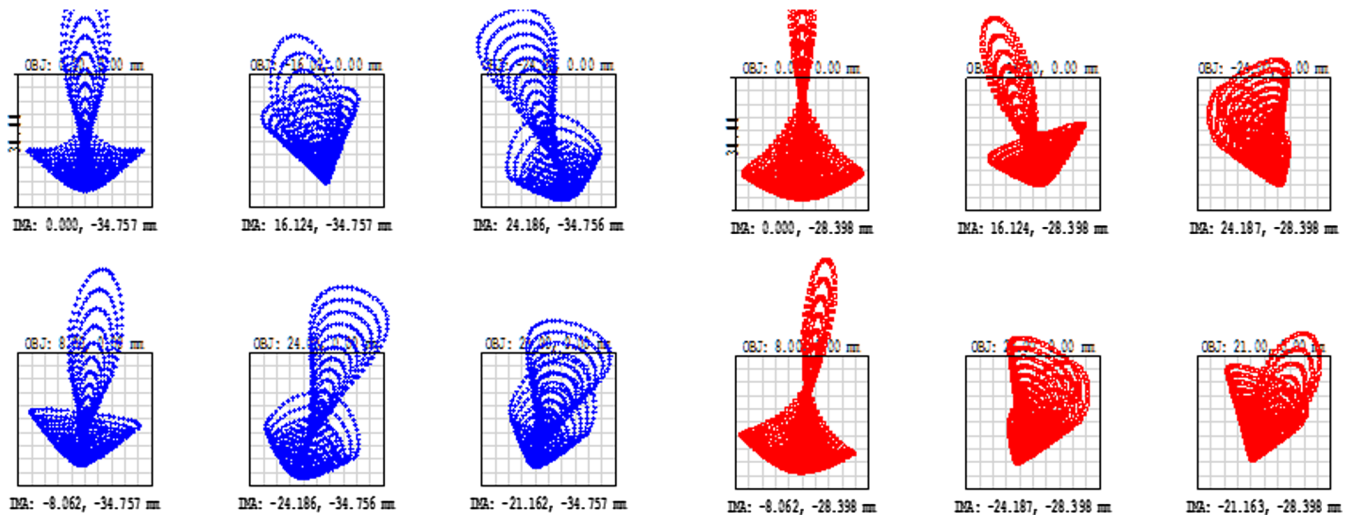


**Fig. 14** Spot diagrams for the shortest and longest wavelength are a good way of demonstrating the coma-like aberration added to the design in order to improve uniformity. A minimum wavefront error (or spot size) solution results in a much less uniform result.

**Table 2** Performance characteristics of the spectrometer of Fig. 11 (design values).

Parameter	Value
<i>F</i> -number	2.8
Slit length	48 mm (1600 × 30 μm)
Spectral range	380 to 2500 nm
Dispersion	10 nm/30 μm
Smile	<0.3% of pixel (<100 nm)
Keystone	<2% of pixel (<600 nm)
Ensquared energy in 30 μm	>0.76
Spectral resolution (SRF FWHM)	<1.35 × sampling
Spatial resolution (CRF FWHM)	<1.1 × sampling
SRF width variation with field	<4.5%
CRF variation with wavelength	<2%

associated with fewer spatial pixels and/or slower optical speed.<sup>23,57</sup> A solid glass Offner has also been demonstrated,<sup>58</sup> which increases throughput although is ultimately limited in achievable slit length for reasonable size and path through the material.

A second spectrometer example spans the same spectral range, 380 to 2500 nm but with 5-nm sampling. This is of the Dyson form<sup>59</sup> and has a single CaF<sub>2</sub> refractive element (Fig. 15). The maximum slit length is 38.4 mm (1280 × 30 μm pixels), although it may also be used with a smaller slit and detector (640 elements) occupying only the top half. The reason for doing so is to avoid detector ghosts, which tend to be more prominent in the Dyson design although they are also present in the Offner design. These are generated by specular reflections from the detector assembly that travel to the grating and return to the detector via a higher order. Generally, order-sorting filters and detector coatings can be used to advantage in mitigating ghost effects<sup>46,60,61</sup> to an acceptable level. A perceived disadvantage of the Dyson form is the proximity of slit and detector; however, this problem has been resolved with appropriate mechanical design<sup>39,62,63</sup> and potentially, the use of a small reflective prism or an in-built reflector to increase the clearance.<sup>39,47,62,64</sup> An advantage of the Dyson form is the

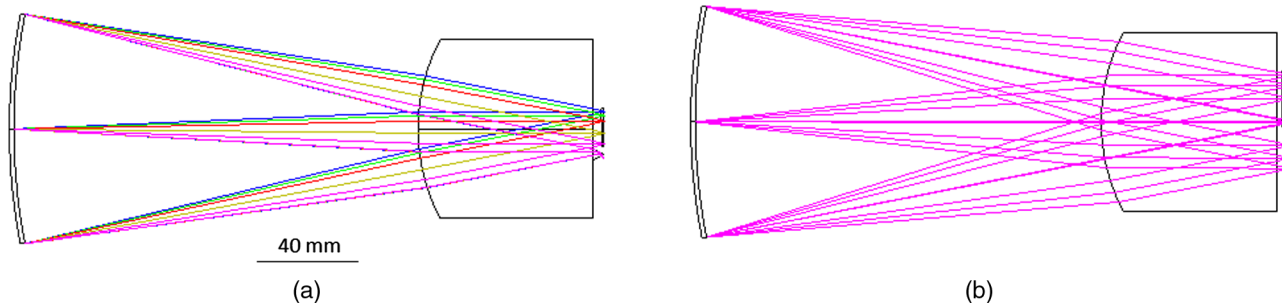
near-normal angle of incidence, which reduces polarization sensitivity. If a beam-folding reflective surface is used, the angle of incidence for all rays is then made greater than the critical angle. With these precautions, <1% polarization sensitivity has been demonstrated.<sup>39</sup> However, if a large slit is sought together with a minimum size design, then the angles of incidence on the curved surface can show significant variation and thus negate the polarization advantage. Minimizing polarization sensitivity is important in the visible/blue end of the spectrum for Earth observations, because the signal arriving at the sensor contains a significant amount of polarized scatter from the atmosphere. Large radiometric errors can therefore result in attempting to remove the atmospheric signal to arrive at the surface reflectance. An interesting solution for reducing polarization sensitivity in a TMA-Offner design has been shown in Ref. 65.

Spot diagrams for the design of Fig. 15 are shown in Fig. 16. There are fewer degrees of freedom in a Dyson than an Offner design, however, the uniformity operands in the merit function still add some aberration in the short wavelength end in order to improve overall uniformity. The design achieves geometric uniformity of >98% in both spatial and spectral directions (smile and keystone <2% of a pixel). The FWHM uniformity is also excellent, with <1% spectral (SRF) variation and <3% spatial (CRF) variation.

The Offner and Dyson designs have also been utilized in the thermal infrared portion of the spectrum. The MERTIS instrument for thermal infrared imaging of Mercury is a TMA/Offner combination operating at  $F/2$ .<sup>66</sup> However, uniformity was not controlled in the design, as evidenced by distortion numbers measured in mm rather than μm. Warren et al.<sup>67</sup> and Johnson et al.<sup>68</sup> utilized the Dyson form and produced fast designs with good uniformity.

## 6 Tolerancing, Assembly, Alignment, and Component Technologies

The achievement of such tight specifications as previously shown requires attention at every step of the process. While recommendations for a design merit function have been provided,<sup>34</sup> the tolerancing process requires the development of new techniques. Geometric uniformity is usually the driver in fabrication and assembly tolerances, and the tolerancing merit function must include smile and keystone operands with appropriate weights. However, there are also systems, where the resolution in terms of FWHM must also be controlled or maximum throughput achieved. Balancing all these demands in the tolerancing and assembly stage requires proper techniques. Early tolerancing methods<sup>69,70</sup>

**Fig. 15** A fast Dyson design utilizing only spherical surfaces.

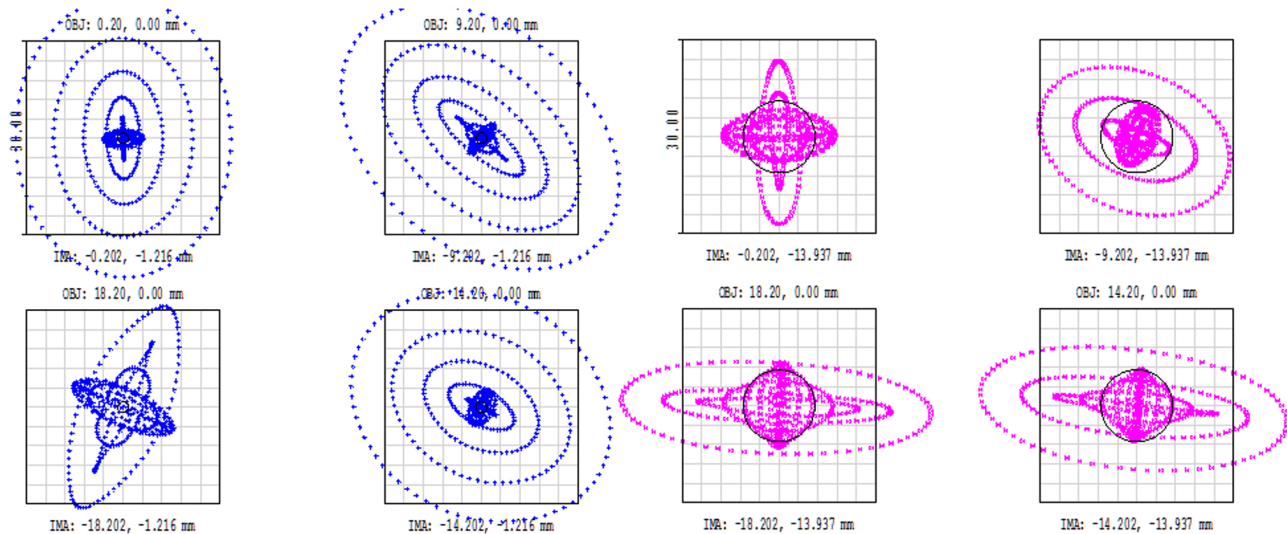


Fig. 16 Spot diagrams for the Dyson design of Fig. 15.

had to be revised in light of ever more demands for high performance. The latest methods<sup>71</sup> are based on the assessment computations and methods of Sec. 4.1.

Alignment techniques for the Offner spectrometers have been described previously.<sup>37,72</sup> They rely on interferometric wavefront measurement, matching the expected wavefront error. The Dyson versions are typically simpler to align and often rely on a single precisely machined alignment tube. Equally critical with the alignment of the optics is the alignment of the detector, which is accomplished through the response function measurements previously described.

Fabrication techniques have varied. The Offner versions have utilized three different athermal constructions: Invar bench with fused silica mirrors, titanium bench with thermally matched glass mirrors, and all-aluminum construction. All three methods have been successful. The Dyson designs have utilized fused silica,  $\text{CaF}_2$  and ZnSe as refractive materials, bonded to titanium or aluminum structures.

The four most critical component technologies for these designs are as follows:

1. Lithographically produced diffraction gratings on curved substrates, with the ability to tailor efficiency over a broad band. Two techniques have been demonstrated at JPL<sup>73–75</sup> but only the electron-beam one has been perfected and placed on flight instruments. Electron-beam gratings have been used on all deployed and flight instruments described here. The technique has continued to mature, having produced gratings of 12 cm in diameter with a sag of several millimeters while minimizing writing artifacts that produce ghosts and scatter. Additionally, an ion-beam etch technique has been reported<sup>76</sup> and diamond turning techniques have also been commercially demonstrated although we know of no reference in the literature.
2. For instruments covering a broad band, the extended response HgCdTe arrays from Teledyne, which also permit snapshot readout thereby eliminating smear artifacts.

3. Lithographically produced slits are critical for achieving the required uniformity since a slit defect is a direct uniformity concern. Slits have been produced using silicon nitride membrane on silicon wafers over lengths of 5 cm while retaining the width and straightness uniformity to within  $\sim 100$  nm. A black silicon etch has been developed with extremely broadband absorption that eliminates ghosts from reflections on the slit substrate.<sup>77</sup>
4. (Commercially available) Order-sorting filters on single substrate that integrate three or four different segments with long pass, short pass, bandpass, or linear-variable transmission.

## 7 Imaging Spectrometer Development at JPL

Several instruments have been successfully developed following the design principles and implementation techniques described in this article (Table 3). These include airborne systems such as MaRS,<sup>78</sup> AVIRIS-ng,<sup>70</sup> HyTES,<sup>68</sup> and PRISM,<sup>39</sup> space mission (M3),<sup>20</sup> and *in-situ* (UCIS).<sup>23</sup> Recently completed and awaiting flight opportunities are the compact wide imaging spectrometer (CWIS)<sup>79</sup> and the snow and water imaging spectrometer (SWIS).<sup>80</sup> The MISE, covering the short and mid-wave infrared region, is part of the Europa Clipper mission and expected to launch in 2022. All these spectrometers with the exception of the first (MaRS) have used a single, extended spectral response focal plane array. Under further development is the Advanced Land Imaging Spectrometer, which could find utility in enhancing Landsat capabilities or as next generation airborne system, as well as systems with freeform surfaces (see Sec. 8). All these designs are of the concentric type, which has proven to be a practically inexhaustible mine of riches, and serve as proof-of-principle for the design techniques and recommendations of this article.

## 8 Advances in Design: Freeform Surfaces

The incorporation of freeform surfaces in a design offers the possibility of reducing the number of surfaces or the overall

**Table 3** Recent imaging spectrometer development at JPL.

System	Design form	Spectral range (nm)	Spectral sampling (nm)	Swath (pixels)	Platform	Application
MaRS	Offner	380–2500	2/4	620	Airborne	Earth
AVIRIS-ng	Offner	380–2500	5	620	Airborne	Earth
M3	Offner	450–3000	10	620	Space	Moon
PRISM	Dyson	350–1050	3	610	Airborne	Earth
HyTES	Dyson	8000–12,000	18	512	Airborne	Earth
UCIS	Offner	450–3000	10	610	In-situ	Earth/Mars
CWIS <sup>a</sup>	Dyson	380–2500	7	1240	Airborne	Earth
SWIS <sup>a</sup>	Dyson	350–1700	6	610	CubeSat	Earth
ALIS <sup>b</sup>	Dyson	380–2500	7	3200	Space/Air	Earth
MISE <sup>b</sup>	Dyson	800–5000	10	300	Space	Europa

<sup>a</sup>Completed and tested, awaiting deployment.

<sup>b</sup>Future, under development.

size or enhancing the field or aperture of a system.<sup>81</sup> We illustrate this with two previously unpublished designs. The first one is a high resolution ( $\lambda/\Delta\lambda \approx 2000$ ) Offner spectrometer derivative with the grating used in Littrow mode, similar to that described in Ref. 52 but for a different spectral region and with a long slit rather than point input. The starting point for this design is an all spherical version with a slit length of 19.2 mm ( $640 \times 30 \mu\text{m}$ ), operating at  $F/4$ . The image quality and uniformity for this design is very good. However, in order to take advantage of recently developed larger focal plane arrays, an attempt was made to double the field (slit length) without affecting the overall spectrometer size by more than a few percent (Fig. 17). Evidently, there are so few degrees of freedom in the design that resorting to a complex mirror shape is the only choice. Conventional aspheric forms were tried and were found to provide insufficient increase in field size. The design became possible with the introduction of a freeform surface that can be described either as an  $x$ - $y$  or a Zernike polynomial surface, with only small to insignificant differences between the two descriptions. A high number of terms were required in both cases. The specifications and performance parameters are shown in Table 4 and Fig. 18.

The second design utilizes a prism as a dispersive element. The impetus for this design is the advent of detectors with customized well depth that can accommodate the variable prism dispersion and associated signal variability across pixels. The additional promise of a prism-based design is higher throughput and lower stray light. However, in order for the throughput advantage to be realized, the prism design must compete with the Dyson grating designs in terms of  $F$ -number and also minimize the number of optical surfaces since, for a broadband system, antireflection coatings will not be very efficient. Generally, prism-based designs are much harder to control for uniformity over a wide field because the prism introduces large aberrations and distortion. Based on these considerations, it was decided to attempt a Dyson-like design with a single lens element and a single prism representing a configuration with the fewest optical elements. The resulting designs (with and without the use of a freeform surface) are not as compact as the corresponding grating designs and cannot readily extend to a similarly high spectral resolution. They nevertheless represent a baseline for this set of specifications until such time as a better design is demonstrated. Both designs cover the same spectral range [380 to 2500 nm, with the same spectral

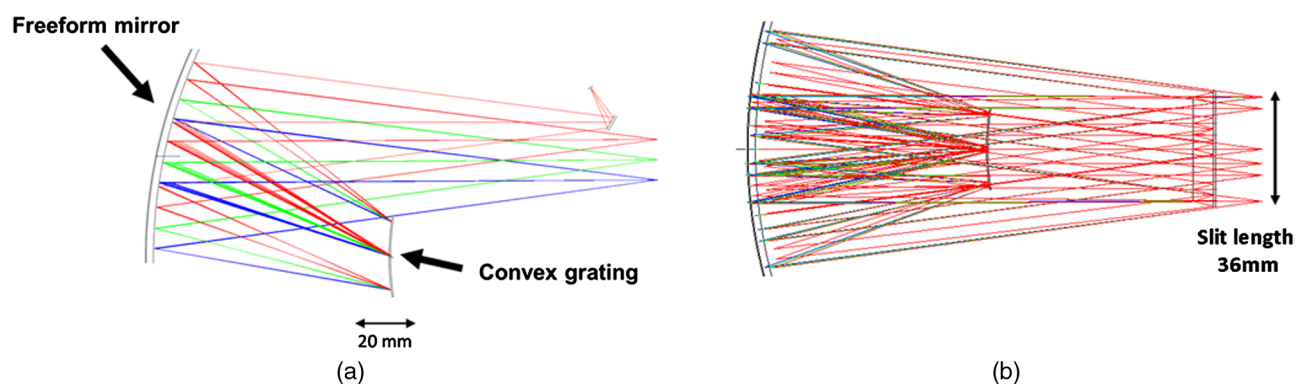


**Fig. 17** A high-resolution Littrow-Offner design with long slit and freeform mirror.

**Table 4** Specification and performance of the spectrometer of Fig. 17.

Parameter	Value
Spectral range (nm)	2000–2400
Spectral sampling (nm)	0.83
Detector pixel ( $\mu\text{m}$ )	$30 \times 30$
Number of spatial pixels	1240
<i>F</i> -number	4
Spot energy in pixel	>83%
Uniformity	>90%
Size (optics)	$90 \times 90 \times 190$ mm

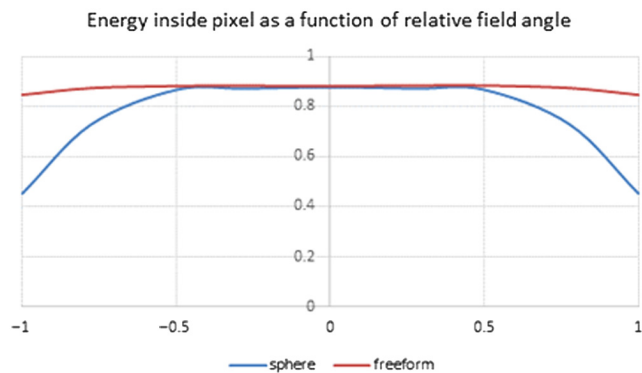


**Fig. 18** Normalized energy inside a  $30 \times 30$  mm pixel as a function of relative field size for an all-spherical and a freeform design of similar size.

sampling (see below)], which are designed for a  $18 \times 18 \mu\text{m}$  pixel size and achieve the same high uniformity.

The design starting point was a Dyson-like spectrometer utilizing a curved Fery prism as the dispersive element (Fig. 19). The design employs a single  $\text{CaF}_2$  lens, which is split into a lens and two prisms for improving detector clearance: a reflective input prism and a transmissive output prism to compensate for the required thickness. The dispersive Fery prism is made of IR-grade fused silica and has the

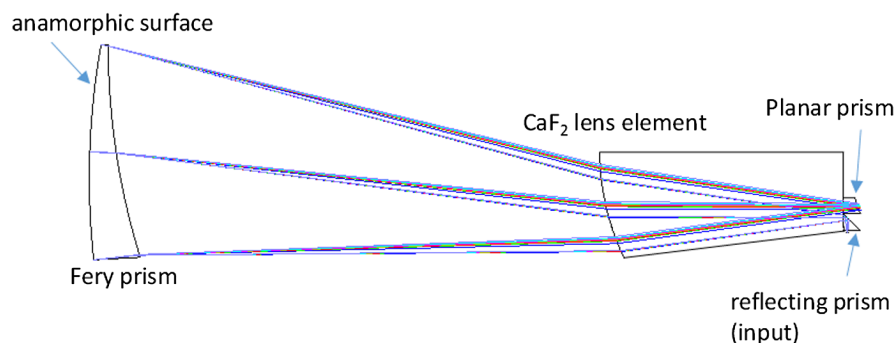


**Fig. 19** A prism-based Dyson design with spherical  $\text{CaF}_2$  lens and a toroidal (anamorphic) reflecting surface.

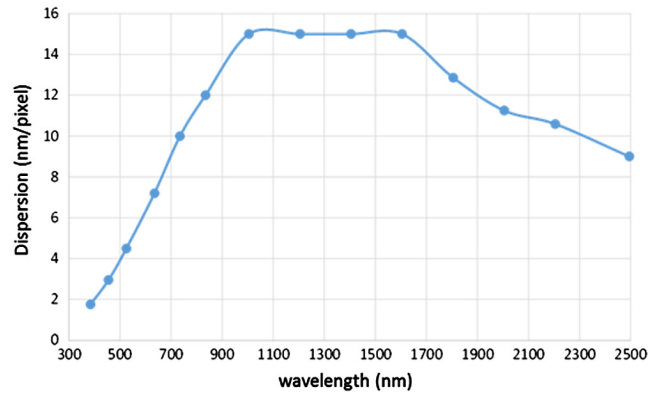


**Fig. 20** Dispersion (in nm per pixel) as a function of wavelength for the design of Fig. 19.

**Table 5** Specifications of a prism Dyson spectrometer and improvement with freeform surface.

Broad-band prism Dyson spectrometer (BPDS)	
Cross-track spatial elements	2160
<i>F</i> -number	2.5
Uniformity	>90%
Optics length	50 cm
Prism diameter	14 cm
BPDS with freeform surface	
Cross-track spatial elements	3200
<i>F</i> -number	2
Uniformity	>90%
Optics length	54 cm
Prism diameter	19.2 cm

rear surface made reflective. The nonlinear character of the dispersion is shown in Fig. 20, where it can be seen that the linear range of constant dispersion is between 1000 and 1600 nm. The maximum sampling condition of <15 nm per pixel has been enforced. The mirror surface is toroidal,

while all other surfaces are spherical or flat. The specifications are shown in Table 5, where they are contrasted with those achieved with the use of a freeform instead of spherical surface on the  $\text{CaF}_2$  element. It may be seen that the length increase is modest, whereas the diameter increase is inevitable due to the increased aperture ( $F/2$  versus  $F/2.5$ ). At the same time, the field (spatial pixels) has increased by  $\sim 50\%$ . Because of the smaller pixel size of this design compared with the previous ones (18 versus  $30\ \mu\text{m}$ ), the uniformity specification while remaining constant as a pixel fraction, actually becomes significantly tighter in absolute terms.

The performance of the freeform design is shown in Fig. 21 in terms of diffraction spot energy inside the pixel for the short and long wavelength, satisfying, if only just, the design principle of  $>75\%$ . In terms of uniformity, the maximum smile is  $0.6\ \mu\text{m}$ , which is remarkable for a slit length of  $57.6\ \text{mm}$ , and yet represents  $3.3\%$  of a  $18\text{-}\mu\text{m}$  pixel, at the upper range of acceptability before tolerancing.

To compensate, the SRF variation through field is very small, at about  $1\%$ , so that the total spectral uniformity (sum of two effects) is better than  $95\%$  at the design stage. The keystone-equivalent error is only  $0.2\ \mu\text{m}$  or  $\sim 1\%$  of a pixel, whereas the worst-case CRF variation through wavelength is  $\sim 5.8\%$ . In tolerancing, it is expected that the smile and keystone errors will be dominant, whereas the SRF and CRF variation will not change considerably.

A more compact design is possible that retains all the performance specifications of the freeform design at the expense of introducing additional surfaces. If we allow the mirror to be separate from the prism so it operates closer to the concentric-aplanatic condition,<sup>82</sup> and if we also introduce a meniscus corrector, the size of the system is reduced to  $\sim 60\%$  of the original while retaining the performance specifications. However, there are now six additional air-glass interfaces, and the resulting drop in transmittance is potentially significant for a broadband system. A raytrace of this more compact system is shown in Fig. 22. For reference, the

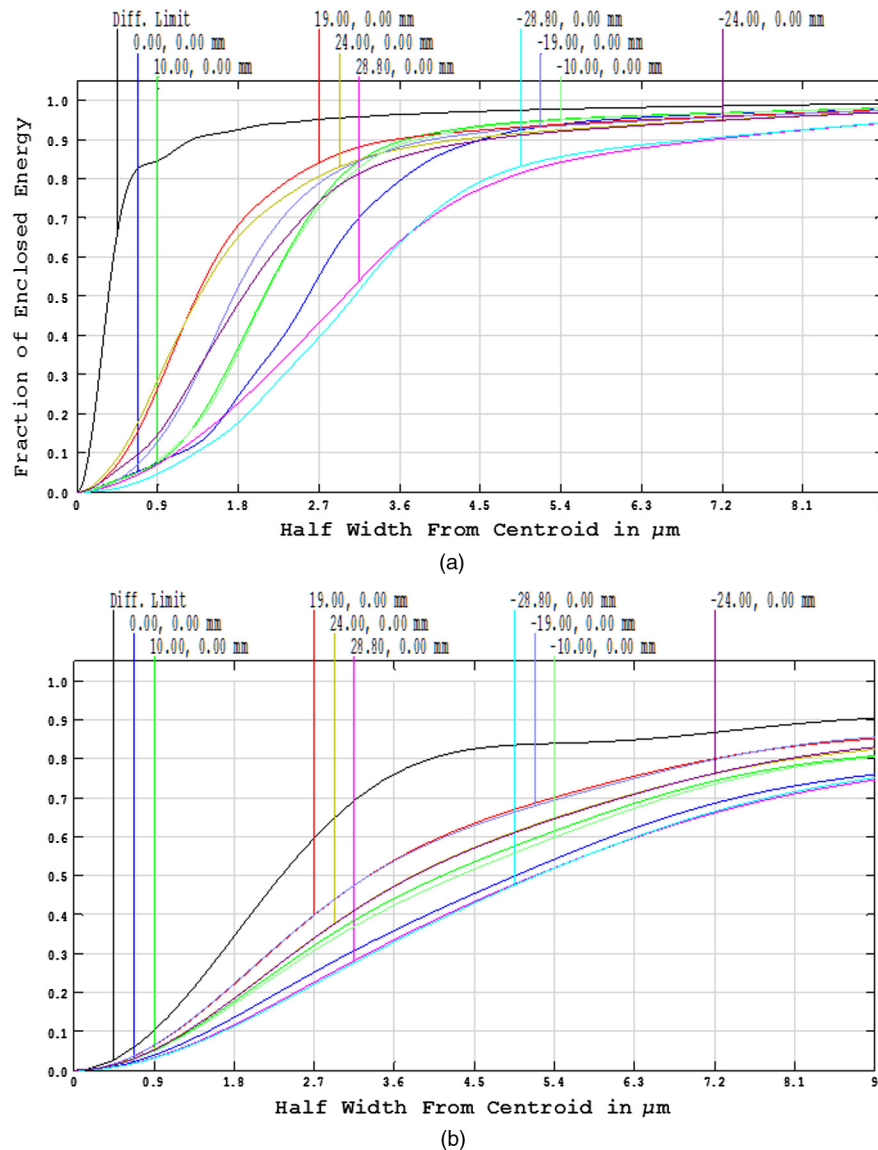


**Fig. 21** Ensquared energy in  $18\text{-}\mu\text{m}$  pixel for the short and long wavelength ends of the spectral range of the freeform prism Dyson design. (a)  $380\text{-nm}$  wavelength and (b)  $2500\text{-nm}$  wavelength. The topmost curve is the diffraction limit. Other curves represent various field points.

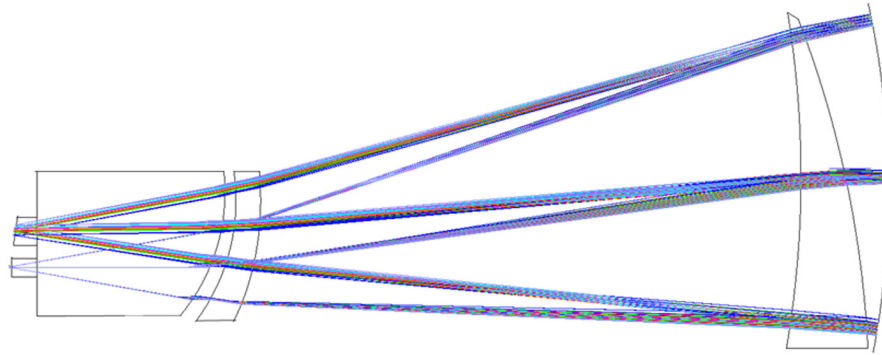


**Fig. 22** A spectrometer design that achieves the same specifications and performance as the freeform system of Table 5, but at ~60% the linear size. The size reduction required a meniscus corrector plate with a sixth order aspheric surface as well as decoupling the mirror from the prism. The prism in this case has spherical surfaces, but the mirror is toroidal. The slit is 58.6 mm long.

prism diameter is 13.6 cm, and the system requires a sixth order asphere in the corrector plate as well as a toroidal mirror. In this case, the freeform surface both enables the design and is likely to become the limiting performance factor as it has almost zero tolerance on beam walk, which means that the pupil location and illumination will have an unexpectedly large effect on image quality. Such effects are minimal or nonexistent with the grating-based systems requiring only spherical or rotationally symmetric surfaces for similar performance.

Alternative prism-based designs are given in Refs. 55, 83, and 84. These are generally high-uniformity designs, although of more modest field and aperture than attempted in this section.

While freeform design offers advantages, the designer should be aware that a lot can be accomplished with spherical surfaces and the occasional conic, which have the advantage of being simple, inexpensive, and easy to align. At the time of writing, freeform designs have not been demonstrated to meet the same stringent specifications as their simpler counterparts in a finished instrument. The real test of freeform surfaces for spectrometer applications rests on meeting the required tolerances in shape and surface finish simultaneously, as well as on achieving the necessary assembly and alignment accuracy using techniques that are yet to be developed.

## 9 Conclusions

We have reviewed the design considerations and principles that underlie the successful implementation of several imaging spectrometer systems employed in a variety of platforms and spanning a broad wavelength range. Design examples were provided to illustrate the application of the principles. The use of freeform surfaces has been shown to extend the design space with successful demonstration of a complete system remaining.

## Disclosures

This work has been supported by several NASA grants. The California Institute of Technology has filed provisional patents for certain aspects of the work described in Sec. 8.

## Acknowledgments

We are grateful to the AVIRIS team, JPL colleagues, and others for their contributions through more than 30 years as well as to our science colleagues, whose science questions and collaboration have provided the impetus for the development of the instruments described here. Within the narrower focus of this paper, we acknowledge Michael Eastwood for pivotal contributions in implementation, Daniel Wilson for unique and innovative diffraction grating design and development, Byron Van Gorp for innovative optomechanical and system design, Victor White and Karl Yee for lithographic slit development, Holly Bender for alignment and assembly contributions, Lori Moore for contributions to tolerancing techniques, Bill Johnson and Simon Hook for HyTES development and Thomas Luchik for unwavering support. The research described here has been performed at the Jet Propulsion Laboratory, California Institute of Technology, under a contract with the National Aeronautics and Space Administration. Reference herein to any specific commercial product, process, or service by trade name, trademark, manufacturer, or otherwise, does not constitute or imply its endorsement by the United States Government or the Jet Propulsion Laboratory, California Institute of Technology.

## References

1. G. Vane, A. F. H. Goetz, and J. B. Wellman, "Airborne imaging spectrometer: a new tool for earth remote sensing," *IEEE Trans. Geosci. Remote Sens.* **22**(6), 546–549 (1984).
2. A. F. H. Goetz et al., "Imaging spectrometry for earth remote sensing," *Science* **228**, 1147–1153 (1985).
3. G. Vane et al., "Airborne visible/infrared imaging spectrometer: an advanced tool for earth remote sensing," in *Proc. IEEE Int. Geoscience and Remote Sensing Symp.*, SP215, pp. 751–757 (1984).
4. G. Vane, "First results from the airborne visible/infrared imaging spectrometer (AVIRIS)," *Proc. SPIE* **834**, 166–174 (1987).
5. R. O. Green et al., "Imaging spectroscopy and the airborne visible/infrared imaging spectrometer (AVIRIS)," *Remote Sens. Environ.* **65**, 227–248 (1998).
6. G. A. Swayze et al., "Mapping advanced argillic alteration at Cuprite, Nevada, using imaging spectroscopy," *Econ. Geol.* **109**(5), 1179–1221 (2014).
7. R. N. Clark et al., "Imaging spectroscopy: earth and planetary remote sensing with the USGS Tetracorder and expert systems," *J. Geophys. Res.* **108**(E12), 5131 (2003).
8. C. M. Lee et al., "An introduction to the NASA Hyperspectral InfraRed Imager (HypIRI) mission and preparatory activities," *Remote Sens. Environ.* **167**, 6–19 (2015).
9. R. W. Carlson et al., "Near-infrared mapping spectrometer experiment on Galileo," *Space Sci. Rev.* **60**(1–4), 457–502 (1992).
10. E. A. Miller et al., "The visual and infrared mapping spectrometer for Cassini," *Proc. SPIE* **2803**, 206–220 (1996).

11. R. H. Brown et al., "The Cassini visual and infrared mapping spectrometer (VIMS) investigation," *Space Sci. Rev.* **115**, 111–168 (2004).
12. J. S. Pearlman et al., "Hyperion, a space-based imaging spectrometer," *IEEE Trans. Geosci. Remote Sens.* **41**, 1160–1173 (2003).
13. M. A. Cutter et al., "Integration and testing of the compact high-resolution imaging spectrometer (CHRIS)," *Proc. SPIE* **3753**, 180–191 (1999).
14. M. K. Barnsley et al., "The PROBA/CHRIS mission: a low-cost smallsat for hyperspectral multiangle observations of the earth surface and atmosphere," *IEEE Trans. Geosci. Remote Sens.* **42**, 1512–1520 (2004).
15. J. P. Bibring et al., "Mars surface diversity as revealed by the OMEGA/Mars express observations," *Science* **307**(5715), 1576–1581 (2005).
16. J. P. Bibring et al., "Global mineralogical and aqueous Mars history derived from OMEGA/Mars express data," *Science* **312**(5772), 400–404 (2006).
17. M. Rast, J. L. Bezy, and S. Bruzzi, "The ESA medium resolution imaging spectrometer MERIS: a review of the instrument and its mission," *Int. J. Remote Sens.* **20**(9), 1681–1702 (1999).
18. S. Murchie et al., "Compact reconnaissance imaging spectrometer for Mars (CRISM) on Mars reconnaissance orbiter (MRO)," *J. Geophys. Res.* **112**(E5), E05S03 (2007).
19. C. M. Pieters et al., "Character and spatial distribution of OH/H<sub>2</sub>O on the surface of the Moon seen by M<sup>3</sup> on Chandrayaan-1," *Science* **326**, 568–572 (2009).
20. R. O. Green et al., "The Moon Mineralogy Mapper (M<sup>3</sup>) imaging spectrometer for lunar science: instrument description, calibration, on-orbit measurements, science data calibration and on-orbit validation," *J. Geophys. Res.* **116**, E00G19 (2011).
21. A. S. K. Kumar et al., "Hyper spectral imager for lunar mineral mapping in visible and near infrared band," *Curr. Sci.* **96**(4), 496–499 (2009).
22. R. B. Lockwood et al., "Advanced responsive tactically-effective military imaging spectrometer (ARTEMIS) development and on-orbit focus," in *IEEE Int. Geoscience and Remote Sensing Symp. (IGARSS)*, Vol. 4, IEEE (2008).
23. B. Van Gorp et al., "Ultra-compact imaging spectrometer for remote, in situ, and microscopic planetary mineralogy," *J. Appl. Remote Sens.* **8**(1), 084988 (2014).
24. R. Greenberger et al., "Imaging spectroscopy of geological samples and outcrops: novel insights from microns to meters," *GSA Today* **25**(12), 4–10 (2015).
25. E. L. Leask and B. L. Ehlmann, "Identifying and quantifying mineral abundance through VSWIR microimaging spectroscopy: a comparison to XRD and SEM," in *IEEE 8th Workshop on Hyperspectral Image and Signal Processing: Evolution in Remote Sensing (WHISPERS)*, Los Angeles, California (2016).
26. J. W. Boardman, F. A. Kruse, and R. O. Green, "Mapping target signatures via partial unmixing of AVIRIS data," in *Summaries of the Fifth Annual JPL Airborne Earth Science Workshop*, pp. 23–26, JPL Publication 95–1 (1995).
27. J. W. Boardman and F. A. Kruse, "Analysis of imaging spectrometer data using n-dimensional geometry and a mixture-tuned matched filtering approach," *IEEE Trans. Geosci. Remote Sens.* **49**, 4138–4152 (2011).
28. G. Swayze et al., "Effects of spectrometer band pass, sampling, and signal-to-noise ratio on spectral identification using the Tetracorder algorithm," *J. Geophys. Res.* **108**(E9), 5105 (2003).
29. S. A. Macenka and M. P. Chrisp, "Airborne visible/infrared imaging spectrometer (AVIRIS) spectrometer design and performance," *Proc. SPIE* **0834**, 32–43 (1987).
30. P. Mouroulis et al., "Optical design of a compact imaging spectrometer for planetary mineralogy," *Opt. Eng.* **46**(6), 063001 (2007).
31. K. D. Mielenz, "Spectroscope slit images in partially coherent light," *J. Opt. Soc. Am.* **57**, 66–74 (1967).
32. P. Mouroulis and R. O. Green, "Spectral response evaluation and computation for pushbroom imaging spectrometers," *Proc. SPIE* **6667**, 66670G (2007).
33. J. F. Silny, "Resolution modeling of dispersive imaging spectrometers," *Opt. Eng.* **56**(8), 081813 (2017).
34. P. Mouroulis, R. O. Green, and T. G. Chrien, "Design of pushbroom imaging spectrometers for optimum recovery of spectroscopic and spatial information," *Appl. Opt.* **39**, 2210–2220 (2000).
35. R. O. Green, "Spectral calibration requirement for earth-looking imaging spectrometers in the solar-reflected spectrum," *Appl. Opt.* **37**, 683–690 (1998).
36. H. A. Bender et al., "Wide-field imaging spectrometer for the hyperspectral infrared imager (HyspIRI) mission," *Proc. SPIE* **9222**, 92220E (2014).
37. H. A. Bender et al., "Alignment and characterization of high uniformity imaging spectrometers," *Proc. SPIE* **8158**, 81580J (2011).
38. D. Schläpfer, J. Nieke, and K. Itten, "Spatial PSF nonuniformity effects in airborne pushbroom imaging spectrometry data," *IEEE Trans. Geosci. Remote Sens.* **45**, 458–468 (2007).
39. P. Mouroulis et al., "Portable remote imaging spectrometer coastal ocean sensor: design, characteristics, and first flight results," *Appl. Opt.* **53**(7), 1363–1380 (2014).
40. T. Skauli, "An upper-bound metric for characterizing spectral and spatial coregistration errors in spectral imaging," *Opt. Express* **20**, 918–933 (2012).
41. J. Fisher and W. C. Welch, "Survey and analysis of fore-optics for hyperspectral imaging systems," *Proc. SPIE* **6206**, 62062R (2006).
42. P. Mouroulis, "Rear landscape on steroids," *Proc. SPIE* **6667**, 666706 (2007).
43. J. M. Rodgers, "Unobscured mirror designs," *Proc. SPIE* **4832**, 33–60 (2002).
44. D. Korsch, *Reflective Optics*, Academic Press, New York (1991).
45. R. Lucke and J. Fisher, "The Schmidt-Dyson: a fast space-borne wide-field hyperspectral imager," *Proc. SPIE* **7812**, 78120M (2010).
46. P. Mouroulis et al., "Landsat swath imaging spectrometer design," *Opt. Eng.* **55**(1), 015104 (2016).
47. P. Mouroulis et al., "A compact, fast, wide-field imaging spectrometer system," *Proc. SPIE* **8032**, 80320U (2011).
48. P. Mouroulis, "Beyond spot diagrams: end-user oriented optical design," *Proc. SPIE* **4832**, 181–185 (2002).
49. L. Mertz, "Concentric spectrographs," *Appl. Opt.* **16**, 3122–3124 (1977).
50. A. Offner, "Unit power imaging catoptric anastigmat," U.S. Patent No. 3, 748, 015 (1973).
51. D. Kwo, G. Lawrence, and M. Chrisp, "Design of a grating spectrometer from a 1:1 Offner mirror system," *Proc. SPIE* **818**, 275–279 (1987).
52. P. Mouroulis, "Optical design of a combined reflectance/Raman confocal microspectrometer," *Proc. SPIE* **4767**, 123–130 (2002).
53. R. L. Lucke, "Out-of-plane dispersion in an Offner spectrometer," *Opt. Eng.* **46**(7), 073004 (2007).
54. X. Prieto-Blanco et al., "The Offner imaging spectrometer in quadrature," *Opt. Express* **18**, 12756–12769 (2010).
55. D. R. Lobb, "Imaging spectrometers using concentric optics," *Proc. SPIE* **3118**, 339–347 (1997).
56. W. Dong, Y.-F. Nie, and J.-S. Zhou, "Design of a concise Féry-prism hyperspectral imaging system based on multi-configuration," *Proc. SPIE* **8910**, 89100B (2013).
57. P. Mouroulis, "Low distortion imaging spectrometer designs utilizing convex gratings," *Proc. SPIE* **3842**, 594–601 (1998).
58. C. P. Warren et al., "Miniaturized visible near-infrared hyperspectral imager for remote-sensing applications," *Opt. Eng.* **51**(11), 111720 (2012).
59. J. Dyson, "Unit magnification optical system without Seidel aberrations," *J. Opt. Soc. Am.* **49**, 713–716 (1959).
60. P. Mouroulis, R. O. Green, and D. W. Wilson, "Optical design of a coastal ocean imaging spectrometer," *Opt. Express* **16**, 9087–9095 (2008).
61. P. Mouroulis et al., "Optical design of a CubeSat-compatible imaging spectrometer," *Proc. SPIE* **9222**, 92220D (2014).
62. H. A. Bender et al., "Snow and water imaging spectrometer (SWIS): optomechanical and system design for a CubeSat-compatible instrument," *Proc. SPIE* **9611**, 961103 (2015).
63. B. Van Gorp et al., "Design of the compact wide swath imaging spectrometer (CWIS)," *Proc. SPIE* **9222**, 92220C (2014).
64. W. R. Johnson et al., "Quantum well earth science testbed," *Infrared Phys. Technol.* **52**, 430–433 (2009).
65. J. Espejo et al., "A hyperspectral imager for high radiometric accuracy earth climate studies," *Proc. SPIE* **8158**, 81580B (2011).
66. G. E. Arnold et al., "Mercury radiometer and thermal infrared spectrometer—a novel thermal imaging spectrometer for the exploration of Mercury," *J. Appl. Remote Sens.* **2**, 023528 (2008).
67. D. W. Warren, D. J. Gutierrez, and E. R. Keim, "Dyson spectrometers for high-performance infrared applications," *Opt. Eng.* **47**(10), 103601 (2008).
68. W. R. Johnson et al., "HyTES: thermal imaging spectrometer development," in *Aerospace Conf.*, Big Sky, Montana, pp. 1–8 (2011).
69. P. Mouroulis, J. J. Shea, and D. A. Thomas, "Design, tolerancing and alignment of pushbroom imaging spectrometers," *Proc. SPIE* **4441**, 106–117 (2001).
70. H. A. Bender et al., "Optical design, performance, and tolerancing of next-generation airborne imaging spectrometers," *Proc. SPIE* **7812**, 78120P (2010).
71. L. B. Moore and P. Mouroulis, "Tolerancing methods and metrics for imaging spectrometers," in *Optical Design and Fabrication*, OSA Technical Digest, paper ITu1A.6, Optical Society of America (2017).
72. P. Mouroulis and M. McKerns, "Pushbroom imaging spectrometer with high spectroscopic data fidelity: experimental demonstration," *Opt. Eng.* **39**, 808–816 (2000).
73. P. D. Maker et al., "New convex grating types manufactured by electron beam lithography," in *Diffraction Optics and Micro-Optics*, Vol. 10, pp. 234–236 (1998).
74. D. Wilson et al., "Recent advances in blazed grating fabrication by electron-beam lithography," *Proc. SPIE* **5173**, 115–126 (2003).
75. P. Mouroulis et al., "Blazed grating fabrication through gray-scale x-ray lithography," *Opt. Express* **11**, 270–281 (2003).
76. Q. Liu et al., "Fabrication of the convex blazed grating," *Proc. SPIE* **7848**, 78480V (2010).

77. P. Mouroulis et al., "Snow and water imaging spectrometer," *ESTF* (2016), [https://esto.nasa.gov/forum/estf2016/PRESENTATIONS/Mouroulis\\_A7P2\\_%20ESTF2016.pdf](https://esto.nasa.gov/forum/estf2016/PRESENTATIONS/Mouroulis_A7P2_%20ESTF2016.pdf)
78. C. Simi, E. Reith, and F. Olchowski, "The mapping reflected-energy sensor-MaRS: a new level of hyperspectral technology," *Proc. SPIE* **7457**, 745703 (2009).
79. B. Van Gorp et al., "Compact wide swath imaging spectrometer (CWIS): alignment and laboratory calibration," *Proc. SPIE* **9976**, 997605 (2016).
80. H. A. Bender et al., "Snow and water imaging spectrometer (SWIS): first alignment and characterization results," *Proc. SPIE* **10402**, 104020A (2017).
81. J. Reimers et al., "Comparison of freeform imaging spectrometer design forms using spectral full-field displays," in *Imaging and Applied Optics*, OSA Technical Digest, paper FM3B.3, Optical Society of America (2015).
82. D. R. Lobb, "Theory of concentric designs for grating spectrometers," *Appl. Opt.* **33**, 2648–2658 (1994).
83. Y. Wang, L. Yuan, and J. Wang, "Optical design of wide swath hyperspectral imager," *Proc. SPIE* **9104**, 910404 (2014).
84. S. Kaiser et al., "Compact prism spectrometer of pushbroom type for hyperspectral imaging," *Proc. SPIE* **7100**, 710014 (2008).

**Pantazis Mouroulis** is a senior research scientist, principal engineer, and supervisor of the Optical Technology Group at Jet Propulsion Laboratory, California Institute of Technology. He received his BS degree from the University of Athens, Greece, and his MSc and PhD degrees from the University of Reading, United Kingdom. His recent research interests have centered on imaging spectroscopy instrumentation and technology. He is a fellow of SPIE and OSA.

**Robert O. Green** is a senior research scientist, fellow, and director of the Microdevices Laboratory at Jet Propulsion Laboratory, California Institute of Technology. He received his PhD degree from the University of California, Santa Barbara. He has been AVIRIS scientist and led the AVIRIS team for over 25 years. He is a coinvestigator in several imaging spectroscopy mission teams, including M3 (Moon orbit), MISE (Europa), CRISM (Mars orbit), and PI of EMIT (Earth orbit).